

NASA TECHNICAL NOTE



NASA TN D-6465

*C.1*

NASA TN D-6465

LOAN COPY: RET  
AFWL (DOG  
KIRTLAND AFB



COMPARISON OF PREDICTED AND  
EXPERIMENTAL WALL TEMPERATURES FOR  
A CYLINDRICAL EJECTOR EXHAUST NOZZLE  
OPERATED WITH A TURBOJET GAS GENERATOR

*by Arthur Lieberman*  
*Lewis Research Center*  
*Cleveland, Ohio 44135*



0133293

1. Report No. NASA TN D-6465	2. Government Accession No.	3. Recipient's Catalog No.	
4. Title and Subtitle COMPARISON OF PREDICTED AND EXPERIMENTAL WALL TEMPERATURES FOR A CYLINDRICAL EJECTOR EXHAUST NOZZLE OPERATED WITH A TURBOJET GAS GENERATOR		5. Report Date August 1971	6. Performing Organization Code
7. Author(s) Arthur Lieberman		8. Performing Organization Report No. E-6300	10. Work Unit No. 720-03
9. Performing Organization Name and Address Lewis Research Center National Aeronautics and Space Administration Cleveland, Ohio 44135		11. Contract or Grant No.	13. Type of Report and Period Covered Technical Note
12. Sponsoring Agency Name and Address National Aeronautics and Space Administration Washington, D. C. 20546		14. Sponsoring Agency Code	
15. Supplementary Notes			
16. Abstract The shroud wall temperatures during operation with and without an afterburner are predicted analytically by using a wall heat balance of hot gas radiation, coolant convection, internal and external radiation, and external free convection. The Hatch-Papell film-cooling correlation predicts an adiabatic wall temperature which is used as the driving temperature for the coolant heat transfer. Ejectors with nozzle area ratios from 1.65 to 2.75 and ejector length to primary diameter ratios from 1.63 to 1.95 were tested. Tests were conducted at nozzle pressure ratios ranging from 2.0 to 6.3, primary total temperatures from 861 to 1939 K (1550 <sup>o</sup> to 3490 <sup>o</sup> R), and corrected secondary weight-flow ratios from 0.027 to 0.088. The predictions yielded reasonably good results throughout the range of conditions tested.			
17. Key Words (Suggested by Author(s)) Coolant slot; Cylindrical ejector; Cylindrical ejector exhaust nozzle; Ejector exhaust nozzle; Exhaust nozzle; Film cooling; Film-cooling correlation; Heat transfer; Nozzle cooling; Shroud cooling		18. Distribution Statement Unclassified - unlimited	
Security Classif. (of this report) Unclassified	20. Security Classif. (of this page) Unclassified	21. No. of Pages 57	22. Price* \$3.00

COMPARISON OF PREDICTED AND EXPERIMENTAL WALL TEMPERATURES  
FOR A CYLINDRICAL EJECTOR EXHAUST NOZZLE OPERATED  
WITH A TURBOJET GAS GENERATOR

by Arthur Lieberman

Lewis Research Center

SUMMARY

An analytical method is developed for predicting the shroud wall temperatures of a cylindrical ejector exhaust nozzle operating with and without an afterburner. These wall temperatures were obtained by applying a heat balance at the wall which included hot gas to wall radiation, convective heat transfer between the coolant stream and the wall, internal wall radiation out the ejector exit, external wall radiation to ambient, and external free convection. Conventional methods were used to predict all terms except the convective heat transfer between the film and wall. This term was evaluated by using the Hatch-Papell semiempirical film-cooling correlation to predict an adiabatic wall temperature. This wall temperature was then used as the driving temperature for heat transfer between the coolant film and the shroud wall.

Results of the analytical procedure are compared with experimental data for a cylindrical ejector nozzle mounted on a nacelle-mounted afterburning turbojet engine in an altitude facility. The ejectors tested had a constant exit area and variable primary area to provide nozzle area ratios from 1.65 to 2.75 and ejector length to primary diameter ratios from 1.63 to 1.95. Tests were conducted at nozzle pressure ratios ranging from 2.0 to 6.3, primary total temperatures from 861 to 1939 K (1550<sup>0</sup> to 3490<sup>0</sup> R), secondary flow total temperatures from 389 to 583 K (700<sup>0</sup> to 1050<sup>0</sup> R), and corrected secondary to primary weight-flow ratios from 0.027 to 0.088.

The analytical predictions yielded reasonably good results at the conditions tested. At the point of maximum recorded wall temperature, the error in predicted values ranged from 27 to -14 percent. The maximum deviation between experimental and predicted temperature was 189 K (340<sup>0</sup> R). At present, the use of the analytical method requires a knowledge of the wall static-pressure distribution for the particular configuration being considered.

## INTRODUCTION

In most supersonic turbojet propulsion systems, some type of ejector is used to pump cooling air over critical engine parts, the primary nozzle, and the ejector shroud. Thus, during operation at high jet exhaust temperatures, film and radiation cooling of the shroud become critical design considerations. Therefore, it is desirable to develop a method of predicting shroud wall temperatures under varying nozzle operating conditions. Various experimental investigations on film cooling of an insulated surface (refs. 1 to 6) provide calculations to evaluate surface temperatures. Reference 7 presented an experimental study on the application of the Hatch-Papell film-cooling correlation to predicting plug and shroud surface temperatures on a plug nozzle at relatively low temperatures. In reference 8 some film-cooling correlations were investigated to determine their applicability to predicting ejector shroud wall temperatures with an engine operating at high-temperature conditions. The Hatch-Papell correlation (ref. 1), used with some changes proposed in reference 6, together with a correction for radiation and free-convection effects, provided the best agreement with measured wall temperatures for a cylindrical ejector operating with a small afterburning turbojet engine at sea-level conditions.

In reference 8 the film-cooling correlation determined an adiabatic wall temperature which was then equated to the wall temperature used in a heat balance of hot gas to wall radiation, wall to coolant forced convection, and inside wall to ambient radiation on an assumed insulated wall. This determined a convective heat-transfer coefficient between the wall and the coolant. This heat-transfer coefficient was assumed applicable to the noninsulated wall and was used in a noninsulated-wall heat balance similar to the insulated case but with outside wall to ambient radiation and outside free convection taken into account. A noninsulated wall temperature was then calculated.

A follow-on investigation over a larger range of operating conditions found this analytical method to have limited application. The method was revised, and the results of a new investigation are presented in this report in detail. Partial preliminary results were previously presented in reference 9. The revised analytical procedure differs from that used in reference 8 mainly in the manner by which the coolant to wall forced-convection heat transfer is determined. Again, as in reference 8, a film-cooling correlation was used to determine an adiabatic wall temperature. The difference between the wall temperature and this adiabatic wall temperature was used in combination with a predicted heat-transfer coefficient based on flat-plate theory to determine the internal convective heat transfer. This convective heat transfer was then used in the noninsulated-wall heat balance. The Hatch-Papell film-cooling correlation (ref. 1) was modified to include an integrated average (from the slot to the point of interest) of heat-transfer coefficient multiplied by shroud internal circumference. This method was suggested in reference 6 and thus differs from that used in reference 8.

The results of the analytical method used in this report are compared with experimental data obtained using a nacelle mounted afterburning turbojet engine with a cylindrical ejector nozzle in an altitude facility. The internal thrust, secondary flow pumping characteristics, secondary flow total-pressure drop, and temperature rise characteristics through the nacelle are reported in reference 10 as ejector 4. A selected variety of test conditions is reported herein as follows: (1) engine operation at maximum afterburning, reheat A, reheat B, and a nonafterburning military setting to provide ejector shroud to primary diameter ratio variations from 1.29 to 1.65 and nozzle exhaust total-temperature variations from 1939 to 861 K (3490<sup>o</sup> to 1550<sup>o</sup> R); (2) nozzle pressure ratio variations from 2.0 to 6.5; and (3) corrected secondary to primary weight-flow ratio variations from 0.027 to 0.088.

## SYMBOLS

A	area
a	absorptivity
C <sub>p</sub>	specific heat at constant pressure
D	diameter
f( )	function of
$\mathcal{F}$	radiation configuration factor
G	gravitational constant
Gr	Grashof number
h	heat-transfer coefficient
J	Joule's constant
k	thermal conductivity
L	mean beam length
l	ejector length
M	Mach number
P	total pressure
Pr	Prandtl number
p	static pressure
q	heat-transfer rate per unit area
R	gas constant

Re	Reynolds number
S	slot height
T	total temperature
Tr	recovery temperature
Tw	wall temperature
$T_w^*$	adiabatic wall temperature
t	static temperature
V	velocity
w	weight-flow rate
x	distance downstream of throat
x'	distance from start of boundary layer
$\alpha$	thermal diffusivity
$\gamma$	ratio of specific heats
$\epsilon$	emissivity
$\mu$	dynamic viscosity
$\rho$	density
$\sigma$	Stefan-Boltzmann constant
$\tau$	temperature ratio, $T_s/T_p$
$\omega$	weight-flow ratio, $w_s/w_p$

Subscripts:

am	ambient radiation conditions
av	average
bl	boundary layer
c	carbon dioxide
f	film
p	primary
s	secondary
sh	shroud
sl	coolant slot
t	throat

w	wall
wa	water vapor
x	distance downstream of throat
x'	distance from start of boundary layer
0	ambient flow conditions
1	hot gas to wall radiation
2	wall to coolant forced convection
3	inside wall to ambient radiation
4	outside wall to ambient radiation
5	outside wall to ambient free convection
7	nozzle inlet
8	nozzle throat
9	nozzle exit

## APPARATUS AND PROCEDURE

### Installation

A schematic view and a photograph of the research hardware installation in the Lewis Research Center Propulsion Systems Laboratory, an altitude engine test facility, are shown in figures 1 and 2, respectively. The installation, test hardware, instrumentation, and test procedures for the ejector investigated herein are reported in greater detail in reference 10 as ejector 4. A General Electric J85-13 turbojet engine was the source of primary flow into the ejector. It was previously calibrated in the same facility (ref. 11). Air entering the engine was metered through a bellmouth venturi. Nozzle exhaust pressure ratio variations were provided independent of the inlet pressure by exhausters controlling the cell pressure. Secondary cooling air was provided from a separate source and metered by standard ASME sharp-edge orifices. This secondary cooling air was introduced upstream of the engine compressor face and passed over the engine outer casing and into the ejector. A small amount of air was discharged into the altitude cell through the bulkhead wall to keep the cell purged of exhaust gases and cooled to an acceptable temperature level.



## Test Hardware and Instrumentation

The J-85 engine had a variable-area primary nozzle that closely approximated a circular geometry. The nozzle area changed with different power settings as the iris primary nozzle translated longitudinally and was accompanied by a change in exit flow convergence angle (ref. 10). A flow diverter (fig. 3) was used to force secondary cooling air underneath the nozzle housing ring and onto the primary leaves.

A photograph of a typical cylindrical ejector configuration with instrumentation is shown in figure 4. Details of the ejector geometry and instrumentation are given in figure 3 and table I. The ejector wall surface had a nominal thickness of 0.16 centimeter (0.063 in.) and was made of Inconel 600. All thermocouples were Chromel-Alumel and those in the secondary passage were radiation shielded. Skin temperatures were measured with the junction of the thermocouple imbedded in the skin, flush with the hot side surface.

## Procedure

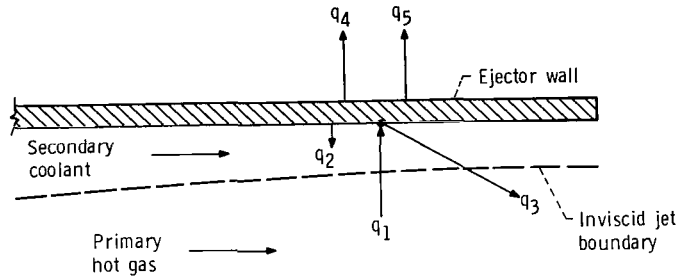
Performance characteristics of the ejector were investigated over a range of primary pressure ratios from 2.0 to 9.0 at corrected secondary to primary weight-flow ratios from 2 to 9 percent and J-85 power settings from approximately 95 percent rated speed to maximum afterburning (ref. 10). Pressure drop and temperature rise characteristics of the secondary flow were also determined. Portions of the data taken in the study of reference 10 were utilized in this investigation and are listed in tables I and II. Conditions upstream of the engine in the plenum chamber were kept relatively constant at  $6.4 \times 10^3$  newtons per square meter (9.3 psia) and 300 K (540° R). A range of predetermined cell ambient pressures was scheduled which resulted in the range of primary nozzle to ambient pressure ratios shown. At each cell pressure, the engine was operated over a range of power settings; at each power setting, secondary weight flow was varied to provide the range of corrected secondary weight flows.

Airflow at the primary airflow measuring station (fig. 1) was determined from static-pressure measurements in the throat of the venturi, a calculated flow coefficient, and total-pressure and total-temperature measurements in the plenum just ahead of the bellmouth lip. With compressor inlet flow, measured total pressure and temperature at the turbine discharge, and measured fuel flow rates known, parameters at station 8 such as total pressure  $P_8$  and temperature  $T_8$  were obtained from previous calibrations (ref. 11).

In the ejector average values of wall static pressure at each particular station as well as average secondary flow conditions were used. Ejector wall temperatures were plotted individually.

## ANALYSIS PROCEDURE

The model used for the cylindrical ejector wall heat balance (similar to ref. 8) is shown in sketch (a). It is assumed that both the temperature gradient across the wall and the axial heat-conduction rate in the wall are negligible and that the heat-transfer areas are equal.



(a) Model used for wall heat balance.

The heat balance on the wall shown in sketch (a) is

$$q_1 = q_2 + q_3 + q_4 + q_5 \quad (1)$$

where the hot gas to wall radiation,  $q_1$  is

$$q_1 = \sigma \frac{\epsilon_w + 1}{2} \left( \epsilon_p t_{p,av}^4 - a_w T_w^4 \right) \quad (2)$$

the wall to coolant forced convection  $q_2$  is

$$q_2 = h_2(T_w - T_w') \quad (3)$$

the inside wall to ambient radiation  $q_3$  is

$$q_3 = \mathcal{F}_3 \sigma \left( T_w^4 - t_{am}^4 \right) \quad (4)$$

the outside wall to ambient radiation  $q_4$  is

$$q_4 = \mathcal{F}_4 \sigma (T_w^4 - t_{am}^4) \quad (5)$$

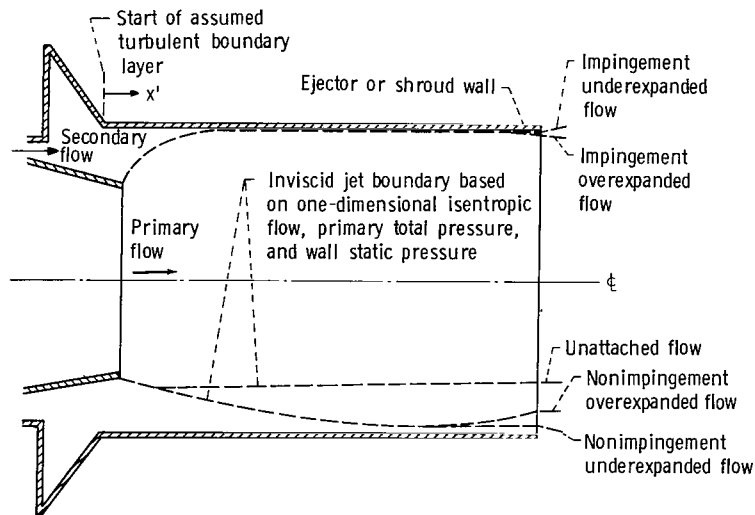
the outside wall to ambient free convection  $q_5$  is

$$q_5 = h_5(T_w - t_0) \quad (6)$$

All the terms in equations (2) to (6) were determined either directly or indirectly as a function of  $T_w$ , as discussed in this section. Equation (1) was then solved by the Newton-Raphson method of iteration to determine the wall temperature assuming an initial estimate of the adiabatic wall temperature  $T_w'$  for  $T_w$ . The values used in equations (2) to (6) were determined as discussed in this section.

### Internal Flow Properties

The primary flow field was determined by assuming that one-dimensional isentropic flow existed and that the measured wall static pressure was uniform across the ejector cross section. The secondary stream was assumed to fill the area remaining between the primary flow field and the ejector wall. The model used for flow and heat transfer is shown in sketch (b). The length  $l$  between the nozzle throat and the end of the ejector (fig. 3) was divided into 10 equal increments. Local flow properties at each of these stations were determined and used in a heat balance. The hot-gas specific-heat ratio  $\gamma_p$  was obtained by matching the hot-gas properties for the ASTMA-1/air mixture to the hot-



(b) Model used for flow and wall heat transfer.

gas static temperature  $t_p$  until the isentropic relations were satisfied. Other properties were then determined either from the gas property tables or the isentropic relations. The secondary stream properties were obtained by assuming that the wall (if insulated) would reach an adiabatic wall temperature  $T'_w$  in accordance with the semi-empirical film-cooling correlation described later and that this  $T'_w$  represented the recovery temperature  $Tr_s$  of the secondary stream. The expression for  $Tr_s$  (ref. 12)

$$T'_w = Tr_s = t_s + Pr_s^{1/3} \frac{V_s^2}{2 C_{p,s} GJ} \quad (7)$$

was used together with the equations of state and continuity and the properties of air to determine the local properties of the secondary stream at each station by iterating until  $t_s$  and the properties agreed. The film-cooling correlation in effect estimates the thermal mixing between the primary and secondary streams.

All secondary flow parameters at the slot inlet located at station 8 (fig. 3) were calculated with the secondary total pressure  $P_s$  and the secondary total temperature  $T_s$  as measured assumed to be applicable at the slot. This is not strictly true, as some heat was probably convected into the secondary stream upstream of the slot because of high nozzle temperatures. An iteration using isentropic equations, continuity, and the properties of air yielded the slot static temperature  $t_{s1}$ , and the slot static pressure  $p_{s1}$ , from which other slot properties were determined as shown in appendix A.

### Hot Gas to Wall Radiation $q_1$

Since the hot gas was made up of the combustion products of ASTMA-1 and air, non-luminous radiation of the combustion products of carbon dioxide and water vapor constituted a significant contribution to the wall heat exchange and had to be considered. In order to solve equation (2) (taken from ref. 13), values for  $t_{p,av}$ ,  $\epsilon_p$ ,  $a_w$ , and  $\epsilon_w$  were required. The hot gas was assumed to radiate at each station at an average static temperature  $t_{p,av}$  obtained by averaging all local hot-gas static temperatures throughout the ejector. Therefore,  $t_{p,av}$  remains constant for each heat balance in a particular ejector. The values of emissivity  $\epsilon_p$  and absorptivity  $a_w$  for hot-gas radiation were estimated as outlined for nonluminous gases in reference 13. The details of calculating  $\epsilon_p$  and  $a_w$  as applicable to the ejectors are presented in appendix B.

The ejector surface was assumed gray. A multiplier factor  $(\epsilon_w + 1)/2$  to correct for this was added to equation (2), which without the factor would apply only to black

bodies. The wall emissivity  $\epsilon_w$  was estimated at 0.65 on the basis of data in reference 14 along with consideration of the color and texture of the surfaces.

### Wall to Coolant Forced-Convection Heat-Transfer Rate $q_2$

The convective heat transfer at the wall, equation (3), was based on the assumption that the potential for heat transfer was the difference between the wall temperature and the adiabatic wall temperature  $T_w'$  of the cooling film in a manner similar to that proposed in reference 15. The  $T_w'$  was determined from the Hatch-Papell correlation at each station as shown in appendix A. Since the slot height for the ejector is large compared to the coolant boundary layer, and the ejector wall has a relatively large diameter, the use of a local heat-transfer coefficient  $h_2$  based on a standard flat-plate correlation for turbulent flow (ref. 12) appeared reasonable. The correlation used was

$$h_2 = 0.0296 \frac{k}{x'} Re_{x'}^{0.8} Pr^{1/3} \quad (8)$$

where fluid properties were evaluated at an average of the adiabatic wall temperature  $T_w'$  and the wall temperature  $T_w$ . The secondary flow boundary layer was assumed turbulent and to originate at the beginning of the cylindrical portion of the nozzle (sketch (b)). The local velocity required for the secondary stream Reynolds number was determined as indicated in the section Internal Flow Properties.

### Inside Wall to Ambient Radiation $q_3$

The internal wall radiation out the exit is given by equation (4) and depends on a local radiation configuration factor  $\mathcal{F}_3$  and the ambient radiation temperature  $t_{am}$ . The configuration factor  $\mathcal{F}_3$  was obtained from figure 5. This figure was derived from data in reference 16 for thermal radiation from the surface of an isothermal cylindrical cavity with gray surfaces. Emissivities of 0.9, 0.75, and 0.5 were presented. As the wall emissivity in the test ejector was assumed to be 0.65, the local configuration factors were interpolated accordingly. The  $t_{am}$  was estimated at the temperature of the surrounding test cell walls. The effects of radiating through the hot gas were assumed small and neglected.

## Outside Surface to Ambient Radiation $q_4$

The external wall radiation is given by equation (5) and depends on a configuration factor and  $t_{am}$ . The configuration factor  $\mathcal{F}_4$  was shown in reference 8 to equal  $\epsilon_w$  for gray bodies as follows. The radiative interchange factor for an enclosed body and its enclosure is given in reference 17 as

$$\mathcal{F}_4 = \frac{\epsilon_w}{1 + \epsilon_w \left( \frac{1}{\epsilon_{am}} - 1 \right) \frac{A_w}{A_{am}}} \quad (9)$$

For the case considered where  $A_{am} \gg A_w$ , equation (9) reduces to

$$\mathcal{F}_4 = \epsilon_w \quad (10)$$

Here again the constant value of  $\epsilon_w = 0.65$  was assumed over the length of the ejector. Since the short outer shroud (fig. 3) was located toward the cool end of the ejector, its effect on  $q_4$  was assumed small and neglected. Again  $t_{am}$  was estimated at the temperature of the surrounding test cell walls.

## Outside Wall to Ambient Free-Convection Heat Transfer $q_5$

The free-convection heat transfer was calculated assuming a horizontal cylinder (ref. 18) wherein the heat-transfer coefficient is given as

$$h_5 = 0.53 \frac{k}{D} (Gr_D Pr)^{1/4} \quad (11)$$

and the properties are obtained at the arithmetic mean temperature  $t_f$  between the wall and ambient air. Equation (11) is valid for Prandtl numbers greater than 0.5 and Grashof numbers ranging from  $10^3$  to  $10^9$ . All cases tested met these limits. The Grashof number was defined as

$$Gr_D = \rho_f^2 G \beta_f (T_w - t_0) \frac{D_{sh}^3}{\mu_f} \quad (12)$$

where  $\beta_f = 1/t_f$ .

## RESULTS AND DISCUSSION

A comparison of experimental and predicted wall temperatures for a cylindrical ejector is presented in figures 6 to 26 for an afterburning turbojet engine operated at maximum reheat, reheat A, reheat B, and military power settings.

Nozzle pressure ratios  $P_8/p_0$  were varied from 2.0 to 6.3 and secondary corrected weight-flow ratios  $(\omega\sqrt{\tau})$  from 0.027 to 0.088. Each of the figures shows (1) the measured static-pressure profile along the ejector wall, (2) the experimental wall temperature measurements, (3) the predicted wall temperatures  $T_w$  as calculated from the heat balance on a noninsulated wall, (4) the predicted adiabatic wall temperature  $T_w'$  calculated by using only the Hatch-Papell film-cooling correlation without taking into account radiation or a wall heat balance, and (5) a cumulative heat distribution of heat in and heat out of the wall in accordance with the wall heat balance assumed in predicting the ejector wall temperature  $T_w$ .

The ejector internal flows can be grouped into five basic configurations, sketch (b), based on data described in reference 19. These five configurations are identified and defined as follows:

(1) Nonimpingement underexpanded flow: This flow pattern occurs at high secondary flows and high nozzle pressure ratios. The expanding primary jet approaches the wall but remains apart from the wall throughout the length of the ejector. Upon leaving the ejector the primary jet expands further. Changes in nozzle pressure ratio affect neither the secondary total-pressure ratio  $P_s/P_p$  nor the ejector wall static-pressure profile. The secondary flow is choked.

(2) Nonimpingement overexpanded flow: This flow pattern occurs at high secondary weight flows and intermediate nozzle pressure ratios. The expanding primary jet approaches the wall, reaches a minimum separation, and then recompresses to match the exit ambient pressure. Changes in nozzle pressure ratio do not affect the secondary total-pressure ratio. The wall pressure profile changes, but the secondary flow remains choked.

(3) Unattached flow: This flow pattern occurs at low nozzle pressure ratios. The primary jet expands slightly, remains separated from the wall, and gradually recompresses to the exit ambient pressure. Changes in nozzle pressure ratio cause the secondary total-pressure ratio, the wall pressure profile, and the secondary weight flow to change.

(4) Impingement underexpanded flow: This flow occurs at low secondary weight flows and high nozzle pressure ratios. The expanding primary jet strikes the ejector wall, remains along the wall, and expands beyond the ejector exit. Changes in nozzle pressure ratio affect neither the ejector pressure ratio nor the ejector wall static-pressure profile. The secondary flow is pumped by mixing with the primary flow (ref. 20).

(5) Impingement overexpanded flow: This flow pattern occurs at low secondary weight flows and intermediate nozzle pressure ratios. The expanding primary jet strikes the wall, remains along the wall but recompresses prior to reaching the ejector exit. Changes in nozzle pressure ratio do not affect the ejector pressure ratio, but the ejector wall static-pressure profile changes beyond the impingement point. The secondary flow is pumped by mixing with the primary flow.

The data in this report have been grouped in accordance with these flow types and are discussed in the order listed. The test conditions for the data presented in this section are summarized in table I.

Secondary flow pumping characteristics (ref. 10, ejector 4) for the ejectors investigated herein indicated that, at a nozzle pressure ratio of 6 and at all power settings, the ejectors were choked (secondary flow was insensitive to further decrease in ambient pressure). At the intermediate nozzle pressure ratio near 3 at maximum reheat, reheat A, and reheat B power settings, the ejector was near the critical nozzle pressure ratio and choked. At the nozzle pressure ratio of 3 and military power setting or at all lower nozzle pressure ratios regardless of power setting, the ejector secondary flows were not choked.

### Nonimpingement Underexpanded Flow

A comparison of calculated and experimental data for an ejector tested at maximum reheat power setting, nozzle pressure ratio of 6.3, and a relatively high corrected secondary weight flow of 0.088 is presented in figure 6. The wall static-pressure profile, figure 6(a), indicates a nonimpingement underexpanded flow since the downstream ejector static pressure does not exceed the secondary total pressure. Reasonably good agreement between predicted wall temperature and measured data (fig. 6(b)) is obtained. The maximum error which occurred at the exit was approximately 181 K (325° R). The scatter in the experimental temperatures was due to nonuniform flow distribution caused by the engine. The initial flat portion of the curves represents the region where the Hatch-Papell correlation predicted that the coolant adiabatic wall temperature was unaffected by heating from the primary stream. Downstream, the predicted adiabatic wall temperature increased rapidly and thus increased the predicted wall temperatures. The cumulative heat distributions into and out of the wall are given in figure 6(c). Up to the ejector location  $x/D_g = 0.86$ , the hot-gas radiation was the only source of heat into the wall. Beyond that point, the predicted coolant-gas adiabatic wall temperatures were higher than the wall temperature, and the convection heat transfer  $q_2$  became a heating factor. However, the adiabatic wall temperatures were always considerably below the primary recovery temperatures because of the insulating effect of the secondary flow.

|||||

Near the ejector exit, the portion of the heat transferred into the wall from internal convection was about three times that due to hot-gas radiation. The wall cooling was achieved primarily through internal radiation out the ejector exit  $q_3$ , and external wall radiation  $q_4$ . Natural convection  $q_5$  provided a small amount of additional cooling.

Comparisons of calculated and experimental data for additional cases of nonimpingement underexpanded flow are presented in figures 7 to 9. Actually these three cases are classified as underexpanded flow, although the wall static-pressure profiles (figs. 7(a), 8(a), and 9(a)) show an overexpansion at the ejector exit. A similar wall pressure profile is shown in figure 11 of reference 19, wherein the wall pressure profile was found to be completely independent of increasing nozzle pressure ratio  $P_8/p_0$ . Additionally, since the last wall static-pressure data point located 1.27 centimeters (1/2 in.) from the exit shows no recompression region, the wall pressure profile cannot significantly change with increasing  $P_8/p_0$ . Therefore, the internal flow will be typical of underexpanded flow as defined in this report. Here again reasonably good agreement between prediction and measured data is observed. At the point of maximum wall temperatures, the error in prediction was 172, 114, and -47 K (310<sup>o</sup>, 205<sup>o</sup>, and -85<sup>o</sup> R) for reheat A, reheat B, and military engine settings, respectively. In general, it appears that for nonimpingement underexpanded flow and the reheat engine settings, wall temperature predictions will be on the high side or conservative. Additionally, when the area ratio  $A_9/A_8$  increases as the total temperature of the primary flow decreases, the primary flow approaches impingement and the predictions become less conservative. For the nonimpingement underexpanded flow cases tested, the errors at the maximum measured temperatures varied from -8 to 25 percent.

### Nonimpingement Overexpanded Flow

Ejector data for conditions of maximum reheat, nozzle pressure ratio of 2.8, and secondary corrected weight-flow ratio of 0.087 are shown in figure 10. The wall pressure profile (fig. 10(a)) is that for nonimpingement overexpanded flow. The measured wall temperatures (fig. 10(b)) were essentially the same as for nonimpingement underexpanded flow (fig. 6(b)). Both cases were taken at the same conditions except for nozzle pressure ratio, which was changed by increasing the back pressure. It appears that, although the internal flow was somewhat different, the measured wall temperature and heat transfer remained essentially the same. Predicted values using the heat balance also remained about the same. For figure 10(b), the maximum error in the calculated wall temperature was 189 K (340<sup>o</sup> R). The predicted heat distribution profile (fig. 10(c)) shows a slightly greater total heat load than figure 6(c). Hot-gas radiation was slightly higher because of a higher average hot-gas temperature. The increase in internal con-

vection  $q_2$  reflects the increased adiabatic wall temperature but the change was relatively small since the heat-transfer coefficient  $h_2$  decreased somewhat.

Comparisons of calculated and experimental data for additional cases of nonimpingement overexpanded flow are presented in figures 11 and 12. There is good agreement between predicted and measured data. At the point of maximum wall temperatures, the error in prediction was 78 and 11 K ( $140^\circ$  and  $20^\circ$  R) for reheat A and reheat B, respectively. In a manner similar to that of the nonimpingement underexpanded flow cases, the predicted temperatures for the reheat settings were on the high side and decreased with increasing area ratio and decreasing total temperature. For the nonimpingement overexpanded flow cases tested, the errors at the maximum measured temperatures varied from 1 to 27 percent.

## Unattached Flow

Ejector data for conditions at maximum reheat, a nozzle pressure ratio of 2.0, and a corrected weight-flow ratio of 0.074 are shown in figure 13. The wall pressure profile (fig. 13(a)) is representative of unattached flow. The predicted maximum uninsulated wall temperature  $T_w$  is 133 K ( $240^\circ$  R) higher than measured at the point of measured maximum temperature. This measured temperature is about 156 K ( $280^\circ$  R) higher than that for maximum reheat nonimpingement flow cases (figs. 6 and 10) and is probably due mainly to the lower secondary weight flow. The increased heat transfer is shown in figure 13(c). Hot-gas radiation increased because of a higher average primary static temperature. Convective heating into the wall increased because of higher adiabatic wall temperatures  $T_w$ . Wall radiation losses  $q_3$  and  $q_4$  and free convection  $q_5$  increased to maintain the heat balance.

Comparisons of calculated and experimental data for additional cases of unattached flow are presented in figures 14 to 19. In all cases agreement is good between predicted and measured data. The error in the  $T_w$  prediction at the point of maximum measured  $T_w$  was 117 and 67 K ( $210^\circ$  and  $120^\circ$  R) for reheat A (fig. 14) and reheat B (fig. 15), respectively. For the military power setting with high secondary weight flow, the errors were 50 K ( $90^\circ$  R) (fig. 16) and 83 K ( $150^\circ$  R) (fig. 17). For the military power setting with low secondary weight flow, the errors were -33 K ( $-60^\circ$  R) (fig. 18) and -22 K ( $-40^\circ$  R) (fig. 19). In general, for the unattached flow cases errors varied from -5 to 16 percent. At the higher secondary weight-flow ratios, the predictions were higher than measured, whereas at the lower secondary weight-flow ratios, the predictions were lower than measured.

A comparison of data for unattached flow (fig. 14) with data for nonimpingement flow (fig. 7) where all operating conditions except nozzle pressure ratio are the same shows

the measured  $T_w$  for the unattached flow to be slightly higher. Predicted wall temperatures were also generally higher except at the ejector exit. Although the hot-gas radiation  $q_1$  (fig. 14(c)) was higher near the exit for the unattached flow case because of the higher primary pressure, the convective heat into the wall  $q_2$  near the exit (fig. 14(c)) was less than for nonimpingement flow (fig. 7(c)) because the heat-transfer coefficient  $h_2$  for the unattached case was sufficiently low to more than offset the higher adiabatic wall temperature  $T'_w$ . Unattached flow (fig. 15) and nonimpingement underexpanded flow (fig. 8) at reheat B settings have essentially the same operating conditions except for nozzle pressure ratio. Again the measured and predicted  $T_w$  are higher for the unattached flow, although no matching of the predicted values at the ejector exit takes place.

### Impingement Underexpanded Flow

Ejector data for conditions at maximum reheat, a nozzle pressure ratio of 6.2, and low corrected weight flow of 0.037 are shown in figure 20. The wall static-pressure profile (fig. 20(a)) is representative of impingement underexpanded flow wherein the primary stream impinged on the wall (ref. 19) at an ejector location of about  $x/D_8 = 0.4$ . Actually, for impingement flow, the wall static pressure is assumed to increase to a value greater than the secondary total pressure. In this case, this assumption is almost true, and therefore the flow has been classified as impingement flow. Good agreement between predicted and measured wall temperatures is observed (fig. 20(b)). The error is 106 K (190° R) at the point of maximum measured temperature. The wall heat distribution (fig. 20(c)) shows the main heat input into the wall to be convective heating  $q_2$ . Hot-gas radiation is comparatively small. The convective cooling  $q_2$  is negligible because of the rapid diffusion of the coolant gas with the hot jet and, in addition, because the entering coolant gas was about 139 K (250° R) hotter than in the previous high-weight-flow case (fig. 13). This higher coolant temperature resulted when the smaller quantity of coolant picked up additional heat while cooling the afterburner. Heat out of the wall is primarily radiation cooling  $q_3$  and  $q_4$  (fig. 20(c)).

Additional comparisons of calculated and experimental data for impingement underexpanded flow are presented in figures 21 to 23. Here again, as in figures 7(a), 8(a), and 9(a), these cases are classified as underexpanded flow, although the wall static-pressure profile shows a slight overexpansion at the ejector exit. As previously explained for these figures, the internal flow is not expected to change with increasing  $P_g/p_0$  and is then typical of underexpanded flow as defined in this report. The ejector wall static-pressure profiles show hot-gas impingement on the wall occurring at  $x/D_8 \approx 0.6$ ,  $x/D_8 \approx 0.75$ , and  $x/D_8 \approx 0.9$  for reheat A, reheat B, and the military

setting, respectively. Good agreement between predicted wall temperature and measured maximum wall temperature was obtained. At the point of measured maximum wall temperature, the error in prediction was  $-11\text{ K} (-20^\circ\text{ R})$  (fig. 21),  $-33\text{ K} (-60^\circ\text{ R})$  (fig. 22), and  $-89\text{ K} (-160^\circ\text{ R})$  (fig. 23) for reheat A, reheat B, and the military setting, respectively. Errors for all cases of impingement underexpanded flow varied from  $-13$  to  $11$  percent. As the  $A_9/A_8$  increased and the total temperature of the primary flow decreased, the predictions varied from too high to too low.

As would be expected, hot-gas radiation  $q_1$  is highest at the maximum reheat setting. At the military setting (fig. 23(c)), the gas radiation exchange acts to cool the wall, although the effect is very small.

## Impingement Overexpanded Flow

Ejector data at conditions of maximum reheat power setting, a nozzle pressure ratio of  $2.8$ , and a corrected coolant weight-flow ratio of  $0.036$  are shown in figure 24. The wall pressure profile (fig. 24(a)) is similar to that of figure 20(a) up to the ejector location  $x/D_8 = 1.1$ , after which a steep recompression region occurs. This ejector is representative of impingement overexpanded flow. Very good agreement between predicted and measured wall temperature is observed (fig. 24(b)). The predicted wall temperature was  $39\text{ K} (70^\circ\text{ R})$  above the maximum measured. Here again, as for the impingement underexpanded flow (fig. 20(c)), the heat distribution into the wall (fig. 24(c)) was primarily convective. The heat out was mainly radiation. The effect of the recompression region in this low-weight-flow case was to cause the predicted convective heat transfer into the wall to level off. The total heat into the wall remained virtually constant in the recompression region. The total heat out of the wall accordingly also remained constant.

Comparisons of calculated and experimental data for additional cases of impingement overexpanded flow are presented in figures 25 and 26. Flow at each engine setting is similar to the impingement underexpanded flow (figs. 21 and 22, respectively) up to the ejector location at which the steep recompression occurs. Agreement between predicted and measured wall temperatures is reasonably good, although on the low side. At the point of measured maximum wall temperature, the error in prediction was  $-111\text{ K} (-200^\circ\text{ R})$  (fig. 25(b)) and  $-128\text{ K} (-230^\circ\text{ R})$  (fig. 26(b)) for reheat A and reheat B settings, respectively. For the three cases of impingement overexpanded flow considered, the errors varied from  $-14$  to  $4$  percent. In general, as  $A_9/A_8$  increased and the primary total temperature decreased, the predictions varied from too high to too low.

In comparing the impingement underexpanded flow to the impingement overexpanded data at each particular value of reheat, the operating conditions were similar except for nozzle pressure ratio. It appears that the steep pressure gradient (fig. 24(a)) toward

the ejector exit causes the measured wall temperatures to remain high, whereas in figure 20(a), where the favorable pressure gradient is longer, the actual wall temperature decreases toward the exit. On the other hand, the predicted temperature profile shows an opposite trend. The same pattern is noted in data for the reheat A and B settings. For the impingement type flow it appears that the wall temperature predictions will be more conservative for the flow with the longer favorable gradient or the underexpanded case. When ejectors with nonimpingement flows are compared to ejectors with impingement flow at the same engine settings, the nonimpingement flow with a longer favorable pressure gradient appears to provide more conservative wall temperature predictions. When unattached flow is compared to impingement flow at the same engine settings, the unattached flow, which has a long, mild adverse pressure gradient, is seen to provide a more conservative wall temperature prediction than impingement flow, which has an initial adverse pressure gradient followed by a favorable pressure gradient.

Figure 27 presents a summary of predicted and measured wall temperatures taken at the point of maximum measured wall temperature for all flow cases considered as a function of nozzle area ratio and primary total temperature. The wall temperature predictions provide reasonably good values throughout the range of power settings and corrected weight flows tested. At the critical maximum reheat power setting, the predictions are conservative in all cases and especially so for the higher corrected weight-flow ratios.

Figure 28 shows the ratio of predicted to maximum measured wall temperature taken at the point of maximum measured wall temperature as a function of nozzle area ratio and primary total temperature. Conservative predictions are representative of data at ratios greater than 1.0, whereas below 1.0, the predictions are low. Again it can be seen that the predictions at the maximum reheat engine settings are slightly conservative at the lower corrected weight-flow ratios. For all types of flow except attached flow, the predictions become less conservative and change to underpredicting as the engine settings change (nozzle area ratio  $A_9/A_8$  increases and primary total temperature decreases). In general, wall temperature predictions for underexpanded flows (higher pressure ratios) are more conservative than predictions for overexpanded flows (lower pressure ratios). Predictions for nonimpingement flows (higher corrected weight flows) are more conservative than predictions for impingement type flows (lower corrected weight flows). Predictions for attached flow cases (lowest pressure ratios) at higher corrected weight-flow ratios are conservative and appear independent of the engine settings.

## CONCLUDING REMARKS

The analytical procedure used herein is based on a previous knowledge of the wall static-pressure profile and on a number of simplifying assumptions. It is likely that the prediction can be improved by further work in the following areas:

1. Use of an axisymmetric method of characteristics to predict the wall static-pressure profile; this would permit wall temperature calculations without any experimental knowledge of the internal flow, and would predict more accurate coolant flow areas and consequently coolant flow properties
2. Development of a film-cooling correlation to predict an adiabatic wall temperature of the film based on an ejector geometry with pressure gradients
3. Use of a wall to coolant flow heat-transfer coefficient based on a flat-plate theory matched to varying secondary flow conditions
4. Use of improved techniques for predicting radiation heat-transfer components

## SUMMARY OF RESULTS

An analytical method of predicting the shroud wall temperature distribution of a cylindrical ejector was compared to experimental data obtained by using a nacelle-mounted afterburning turbojet engine in an altitude test facility. The predicted data were obtained by combining an evaluation of the heat transfer due to radiation and convection with a slight modification of an existing film-cooling correlation. The cylindrical ejectors had nozzle area ratios varying from 1.65 to 2.75 and ejector length to primary diameter ratios from 1.63 to 1.95. Data were obtained at corrected secondary to primary weight-flow ratios ranging from 0.027 to 0.088, nozzle pressure ratios from 2.0 to 6.3, primary total temperatures from 861 to 1939 K (1550<sup>o</sup> to 3490<sup>o</sup> R), and secondary flow total temperatures from 389 to 583 K (700<sup>o</sup> to 1050<sup>o</sup> R). It is concluded that

1. In general, the calculated wall temperatures matched the data reasonably well. Deviations of the calculated wall temperatures from the data ranged from 27 to -14 percent at the point of maximum recorded wall temperature.
2. In general, at the maximum reheat engine settings (small area ratio) the calculated wall temperatures matched the data better for cases where the nozzle had impingement-type internal flow (low corrected weight flows and higher nozzle pressure ratios) than for cases with either nonimpingement flow (high corrected weight-flow ratios and higher nozzle pressure ratios) or unattached flow (low nozzle pressure ratios).
3. In general, as the reheat engine setting was reduced (nozzle area ratio increased and primary total temperature decreased), the error in predicted wall temperature decreased and then became increasingly negative for each of the particular types of internal

flow conditions considered except unattached flow. In the latter case, the error remained relatively constant with varying engine setting.

4. In general, nonimpingement flow with a longer favorable pressure gradient as compared to impingement-type flow tended to provide more conservative wall temperature predictions. Unattached flow with a mild adverse pressure gradient tended to provide more conservative predictions than the impingement-type flow with an initial adverse pressure gradient followed by a favorable pressure gradient. Underexpanded flow with a more favorable pressure gradient than overexpanded flow tended to provide more conservative wall temperature predictions.

Lewis Research Center,  
National Aeronautics and Space Administration,  
Cleveland, Ohio, May 13, 1971,  
720-03.

## APPENDIX A

### DETERMINATION OF ADIABATIC WALL TEMPERATURE $T_w$

The adiabatic wall temperature at each station was determined from the adiabatic wall film-cooling correlation proposed in reference 1 and modified to use an integrated average heat-transfer coefficient  $h_{f,av}$ . Reference 6 found that the integrated average provided a better correlation for a rocket nozzle. Since the pressure gradients in the ejector were more like those in a rocket nozzle than the original zero pressure gradient model, the averging technique was used. The correlation is

$$\ln\left(\frac{T_{r_p} - T_w}{T_{r_p} - t_{sl}}\right) = - \left( \frac{\pi D_{sh} h_{f,av} x}{w_s C_{p,sl}} - 0.04 \right) \left( \frac{S V_{p,t}}{\alpha_{sl}} \right)^{0.125} f \left( \frac{V_{p,t}}{V_{sl}} \right) \quad (A1)$$

where

$$h_f = 0.0265 \frac{k_f}{D_{sh}} Re_f^{0.8} Pr_f^{0.3} \quad (A2)$$

$$f\left(\frac{V_{p,t}}{V_{sl}}\right) = 1 + 0.4 \tan^{-1}\left(\frac{V_{p,t}}{V_{sl}} - 1\right) \quad \text{for } \frac{V_{p,t}}{V_{sl}} \geq 1.0 \quad (A3)$$

The primary flow field was determined as shown in the section ANALYSIS PROCEDURE. The local hot-gas recovery temperature  $T_{r_p}$  was determined at a distance  $x$  downstream of the throat (fig. 3) by the expression (ref. 12)

$$T_{r_p} = \left( 1 - Pr_p^{1/3} \frac{\gamma_p - 1}{2} M_p^2 \right) t_p \quad (A4)$$

The primary Mach number  $M_p$  and specific-heat ratio  $\gamma_p$  at the distance  $x$  were obtained by assuming a  $\gamma_p$  and solving for  $M_p$  in the isentropic equation

$$\frac{p_p}{P_p} = \left( 1 + \frac{\gamma_p - 1}{2} M_p^2 \right)^{-\frac{\gamma_p}{\gamma_p - 1}} \quad (A5)$$

The static temperature  $t_p$  was then calculated from

$$t_p = T_p \left( 1 + \frac{\gamma_p - 1}{2} M_p^2 \right)^{-1} \quad (A6)$$

Using  $t_p$  and the properties tables gave a revised  $\gamma_p$  for the ASTMA-1/air mixture, and the calculation was repeated until  $\gamma_p$  agreed with  $t_p$ . The Prandtl number  $Pr_p$  was then obtained from the property tables at the final  $t_p$ .

All secondary flow parameters ( $t_{sl}$ ,  $w_{sl}$ ,  $C_{p,sl}$ ,  $\alpha_{sl}$ , and  $V_{sl}$ ) were taken at slot exit conditions (station 8, fig. 3) and were calculated from the equation of continuity

$$M_{sl} = \frac{w_{sl}}{\rho_{sl} A_{sl} \sqrt{\gamma_{sl} G R t_{sl}}} \quad (A7)$$

A value of  $M_{sl}$  was calculated by assuming  $T_s$  and  $P_s$  for  $t_{sl}$  and  $p_{sl}$ ,  $\gamma_{sl}$  and the density  $\rho_{sl}$  from the property tables at  $t_{sl}$  and  $p_{sl}$ , and  $A_{sl}$  from geometry. This value of  $M_{sl}$  together with  $\gamma_{sl}$ ,  $P_{sl}$ , and  $T_{sl}$  was then used in equations (A5) and (A6) to determine a revised  $t_{sl}$  and  $p_{sl}$ . This procedure was repeated until  $t_{sl}$  and  $p_{sl}$  did not change. The property values for  $C_{p,sl}$  and  $\alpha_{sl}$  were then determined from air property tables.

A local heat-transfer coefficient  $h_{f,x}$  (eq. (A2)) was determined by using air fluid properties evaluated at a temperature  $t_f$  equal to an average of the local primary static temperature and the secondary slot inlet static temperature. The Reynolds number was based on

$$Re_f = \frac{\rho_f V_p D_{sh}}{\mu_f} \quad (A8)$$

where  $V_p$  is the local primary velocity. The local heat-transfer coefficients were averaged from the throat to station  $x$  to obtain  $h_{f,av}$ . Since  $D_{sh}$  is constant for the ejector, the term  $\pi D_{sh} h_{f,av}$  represents the integrated average of the heat-transfer

coefficient multiplied by the shroud internal circumference as suggested in reference 6.

The primary throat velocity  $V_{p,t}$  was calculated from the isentropic expression

$$V_{p,t} = \sqrt{\gamma_{p,t} R G T_{p,t}} \quad (A9)$$

where  $t_{p,t}$  and  $\gamma_{p,t}$  were determined from equation (B6) ( $M = 1$ ) and ASTMA-1/air mixture property tables by iteration until  $\gamma_p$  and  $t_p$  agreed.

## APPENDIX B

### DETERMINATION OF $\epsilon_p$ AND $a_w$

The values of the hot-gas emissivity  $\epsilon_p$  and wall absorptivity  $a_w$  were calculated essentially as presented in reference 13:

$$\epsilon_p = \epsilon_c C_c + \epsilon_{wa} C_{wa} - \Delta\epsilon \quad (B1)$$

$$a_w = a_c + a_{wa} - \Delta a \quad (B2)$$

where

$$\epsilon_c = f(t_p, p_c L)$$

$C_c$  correction for total-pressure effect for carbon dioxide

$$\epsilon_{wa} = f(t_p, p_{wa} L)$$

$C_{wa}$  correction for total-pressure effect for water vapor

$\Delta\epsilon$  correction for a mixture of carbon dioxide and water vapor

$$a_{wa} = f\left(T_w, p_w L \frac{T_w}{t_p}\right) \left(\frac{t_p}{T_w}\right)^{0.45} C_{wa}$$

$$a_c = f\left(T_w, p_c L \frac{T_w}{t_p}\right) \left(\frac{t_p}{T_w}\right)^{0.65} C_c$$

$\Delta a$  correction for mixture of carbon dioxide and water vapor

The various parameters were determined in the following manner. The hot-gas jet was assumed to expand isentropically in the ejector to match the measured wall pressure profile. An average hot-gas static temperature and average static pressure over the ejector length was then calculated by averaging the local station values (see the section ANALYSIS PROCEDURE). These average values, the fuel-air ratio, and the method of reference 21 were used to determine mole fractional values for the products of combustion with the products assumed to have equilibrium composition. The average hot-gas static pressure was multiplied by the mole fractions to obtain a partial pressure for the carbon dioxide and water vapor. The mean beam length  $L$  was estimated with the use of the table in reference 13. The  $P_G L$  factor (ref. 13) was assumed equal to zero since the partial pressures were very low. The hot gases were assumed at constant density and approxi-

mately formed a radiating cylinder which extended out the ejector exit and to some extent into the primary throat so that a mean beam length factor halfway between that of an infinite cylinder and a right circular cylinder (height equal to diameter) radiating to the whole surface was assumed at a value of 0.83. The characterizing dimension  $X$  (ref. 13) was chosen at a calculated average jet diameter for the ejector. This average jet diameter was determined by calculating the local primary jet diameter (see the section ANALYSIS PROCEDURE) at each of 10 equally spaced stations from the nozzle throat to the end of the ejector and averaging them. The mean beam length  $L$  is then a product of the average jet diameter and 0.83. The partial pressure of the carbon dioxide or of the water vapor, whichever is applicable, was multiplied by the mean beam length to give  $p_c L$  or  $p_{wa} L$ . Using these factors and the average hot-gas static temperature,  $\epsilon_c$  and  $\epsilon_{wa}$  at each station were determined from the charts of reference 13.

Because of the comment (ref. 22) that the total-pressure corrections  $C_c$  and  $C_{wa}$  did not possess a high degree of accuracy for pressures different from 1 atmosphere, these corrections were omitted. The corrections for the interaction of carbon dioxide and water vapor ( $\Delta\epsilon$ ) were found to be negligible and assumed 0. Then, from equation (A1),  $\epsilon_p$  equals  $\epsilon_c + \epsilon_{wa}$ . Since an average hot-gas static temperature and average hot-gas partial pressure of carbon dioxide and water vapor are used,  $\epsilon_p$  is the same for any ejector cross section. On the other hand,  $a_w$  is different at each station, since it depends on  $T_w$ . Values of  $a_c$  and  $a_{wa}$  were obtained from charts (ref. 13) as functions of  $T_w$  and  $p_c L(T_w/t_p)$  or  $p_{wa} L(T_w/t_p)$ . The values were corrected by multiplying by  $(t_p/T_w)^{0.65}$  or  $(t_p/T_w)^{0.45}$  as applicable (eq. (B2)) to obtain  $a_c$  and  $a_{wa}$ , respectively. Again  $C_c$  and  $C_{wa}$  were assumed to equal 1, and  $\Delta a$  was set equal to 0.

## REFERENCES

1. Hatch, James E.; and Papell, S. Stephen: Use of a Theoretical Flow Model to Correlate Data for Film Cooling or Heating an Adiabatic Wall by Tangential Injection of Gases at Different Fluid Properties. NASA TN D-130, 1959.
2. Weighardt, K.: Hot-Air Discharge for De-Icing. Translation F-TS-919-Re, Air Material Command, Dec. 1946.
3. Chin, J. H.; Skirvin, S. C.; Hayes, L. E.; and Silver, A. H.: Adiabatic Wall Temperature Downstream of a Single, Tangential Injection Slot. Paper 58-A-107, ASME, 1958.
4. Seban, R. A.; Chan, H. W.; and Scesa, S.: Heat Transfer to a Turbulent Boundary Layer Downstream of an Injection Slot. Paper 57-A-36, ASME, 1957.
5. Goldstein, R. J.; Eckert, E. R. G.; Tsou, F. K.; and Haji-Sheikh, A.: Film Cooling With Air and Helium Injection Through a Rearward-Facing Slot Into a Supersonic Air Flow. Rep. HTL TR No. 60, University of Minnesota, Feb. 1965.
6. Lucas, James G.; and Golladay, Richard L.: Gaseous-Film Cooling of a Rocket Motor With Injection Near the Throat. NASA TN D-3836, 1967.
7. Chenoweth, Francis C.; and Lieberman, A.: Experimental Investigation of Heat-Transfer Characteristics of a Film-Cooled Plug Nozzle With Translating Shroud. NASA TN D-6160, 1971.
8. Chenoweth, Francis C.; and Steffen, Fred W.: Comparison of Experimental and Predicted Heat-Transfer Characteristics for a Cylindrical Ejector. NASA TM X-1641, 1968.
9. Chenoweth, Francis C.; and Lieberman, Arthur: Prediction of Heat-Transfer Characteristics for Ejector Exhaust Nozzles. Analytic Methods in Aircraft Aerodynamics. NASA SP-228, 1970, pp. 623-638.
10. Samanich, Nick E.; and Huntley, Sidney C.: Thrust and Pumping Characteristics of Cylindrical Ejectors Using Afterburning Turbojet Gas Generator. NASA TM X-52565, 1969.
11. Antl, Robert J.; and Burley, Richard R.: Steady-State Airflow and Afterburning Performance Characteristics of Four J85-GE-13 Turbojet Engines. NASA TM X-1742, 1970.
12. Rohsenow, Warren M.; and Choi, Harry Y.: Heat, Mass, and Momentum Transfer. Prentice-Hall, Inc., 1961.

13. McAdams, Willaim H.: Heat Transmission. Third ed., McGraw-Hill Book Co., Inc., 1954.
14. Wolf, J., ed.: Aerospace Structural Metals Handbook. Vol. IIA. Non-Ferrous Alloys. Belfour Stulen, Inc. (AFML-TR-68-115), 1968.
15. Hartnett, J. P.; Birkebak, R. C.; and Eckert, E. R. G.: Velocity Distributions, Temperature Distributions, Effectiveness and Heat Transfer for Air Injected Through a Tangential Slot into a Turbulent Boundary Layer. J. Heat Transfer, vol. 83, no. 3, Aug. 1961, pp. 293-306.
16. Sparrow, E. M.; Albers, L. U.; and Eckert, E. R. G.: Thermal Radiation Characteristics of Cylindrical Enclosures. J. Heat Transfer, vol. 84, no. 1, Feb. 1962, pp. 73-81.
17. Jakob, Max: Heat Transfer. Vol. 2, John Wiley & Sons, Inc., 1957.
18. Kreith, Frank: Principles of Heat Transfer. Second ed., International Textbook Co., 1965.
19. Kochendorfer, Fred E.; and Rousso, Morris D.: Performance Characteristics of Aircraft Cooling Ejectors Having Short Cylindrical Shrouds. NASA RM E51E01, 1951.
20. Beheim, Milton A.; Anderson, Bernhard H.; Clark, John S.; Corson, Blake W., Jr.; Stitt, Leonard E.; and Wilcox, Fred A.: Supersonic Exhaust Nozzles. Aircraft Propulsion. NASA SP 259, 1971, pp. 233-282.
21. Zeleznik, Frank J.; and Gordon, Sanford: A General IBM 704 or 7090 Computer Program for Computation of Chemical Equilibrium Compositions, Rocket Performance, and Chapman-Jouguet Detonations. NASA TN D-1454, 1962.
22. Hottel, H. C.; and Egbert, R. B.: Radiant Heat Transmission from Water Vapor. Trans. AIChE, vol. 38, no. 3, June 25, 1942, pp. 531-568.

TABLE I. - EJECTOR TEST CONDITIONS AND GEOMETRY

Figure	Power setting	Fuel-air ratio	Nozzle pressure ratio, $P_8/p_0$	Corrected weight flow, $\omega \sqrt{\tau}$	Length-diameter ratio, $l/D_8$	Primary flow				Secondary flow				Nozzle area ratio, $A_9/A_8$
						Throat diameter, $D_8$		Throat area, $A_8$		Slot height, $S$		Slot area, $A_{sl}$		
						cm	in.	cm <sup>2</sup>	in. <sup>2</sup>	cm	in.	cm <sup>2</sup>	in. <sup>2</sup>	
6	Maximum	0.057	6.3	0.088	1.63	38.53	15.17	459.7	181.0	5.6	2.2	304.3	119.8	1.66
7	A	.043	6.3	.067	1.68	36.65	14.43	414.8	163.3	6.6	2.6	344.7	137.5	1.84
8	B	.035	6.5	.069	1.66	34.93	13.75	376.4	148.2	7.4	2.9	387.6	152.6	2.03
9	Military	-----	6.4	.073	1.94	30.28	11.92	283.0	111.4	9.6	3.8	481.1	189.4	2.70
10	Maximum	.057	2.8	.087	1.63	38.53	15.17	458.5	180.5	5.6	2.2	305.6	120.3	1.67
11	A	.044	2.9	.063	1.69	36.68	14.44	415.8	163.7	6.6	2.6	348.2	137.1	1.84
12	B	.036	2.9	.059	1.66	34.93	13.75	376.9	148.4	7.4	2.9	387.1	152.4	2.03
13	Maximum	.056	2.0	.074	1.64	38.48	15.15	456.4	179.7	5.6	2.2	307.6	121.1	1.67
14	A	.042	2.0	.067	1.71	36.14	14.23	404.1	159.1	6.9	2.7	359.9	141.7	1.89
15	B	.035	2.0	.068	1.69	34.85	13.72	374.4	147.4	7.4	2.9	389.6	153.4	2.04
16	Military	.018	3.0	.078	1.95	30.07	11.84	278.4	109.6	9.9	3.9	485.6	191.2	2.74
17	Military	.018	2.1	.076	1.94	30.07	11.84	279.4	110.0	9.9	3.9	484.6	190.8	2.73
18	Military	.018	2.9	.033	1.94	30.18	11.88	279.6	110.1	9.6	3.8	484.4	190.7	2.73
19	Military	.018	2.1	.033	1.94	30.07	11.84	279.9	109.4	9.9	3.9	486.2	191.4	2.75
20	Maximum	.057	6.2	.037	1.63	38.66	15.22	461.5	181.7	5.6	2.2	302.5	119.1	1.66
21	A	.043	6.3	.027	1.69	36.63	14.42	415.3	163.5	6.6	2.6	349.8	137.7	1.84
22	B	.036	6.4	.028	1.66	34.85	13.72	375.4	147.8	7.4	2.9	388.6	153.0	2.04
23	Military	-----	6.4	.032	1.94	30.28	11.92	284.2	111.9	9.6	3.8	479.8	188.9	2.69
24	Maximum	.057	2.8	.036	1.63	38.66	15.22	461.8	181.8	5.6	2.2	302.3	119.0	1.65
25	A	.044	2.8	.027	1.69	36.65	14.43	414.5	163.2	6.6	2.6	349.5	137.6	1.84
26	B	.035	2.9	.029	1.66	34.93	13.75	376.2	148.1	7.4	2.9	387.9	152.7	2.03

TABLE II. - EJECTOR FLOW GEOMETRY<sup>a</sup>

Figure	Power setting	Primary flow						Secondary flow						Ambient static pressure, $P_0$	
		Total pressure, $P_p$		Total temperature, $T_p$		Weight flow, $w_p$		Total pressure, $P_s$		Total temperature, $T_s$		Weight flow, $w_s$			
		N/cm <sup>2</sup> abs	psia	K	°R	kg/sec	lb/sec	N/cm <sup>2</sup> abs	psia	K	°R	kg/sec	lb/sec	N/cm <sup>2</sup> abs	psia
6	Maximum	12.4	18.0	1924	3464	12.94	28.52	5.05	7.32	395	711	3.95	5.56	1.98	2.87
7	A	12.5	18.2	1639	2950	12.87	29.38	3.93	5.70	420	756	2.57	3.73	2.00	2.90
8	B	12.8	18.5	1434	2582	12.77	28.16	3.56	5.16	413	744	2.53	3.67	1.98	2.87
9	Military	12.8	18.5	881	1585	12.02	26.50	2.61	3.78	402	723	1.99	2.88	1.97	2.86
10	Maximum	12.3	17.8	1933	3480	12.87	28.37	5.10	7.39	393	708	3.78	5.48	4.41	6.39
11	A	12.7	18.4	1674	3013	12.90	28.44	3.96	5.75	426	767	2.45	3.56	4.41	6.39
12	B	12.8	18.5	1451	2612	12.71	28.03	3.52	5.10	427	768	2.22	3.22	4.39	6.36
13	Maximum	12.3	17.8	1940	3492	12.76	28.14	5.90	8.56	414	745	3.12	4.52	6.20	8.99
14	A	12.5	18.2	1634	2941	12.68	27.95	5.70	8.26	423	762	2.52	3.65	6.21	9.01
15	B	12.7	18.4	1438	2589	12.58	27.73	5.75	8.34	433	779	2.38	3.45	6.18	8.96
16	Military	12.8	18.6	895	1611	11.90	26.23	4.23	6.13	444	800	1.99	2.89	4.37	6.34
17	Military	13.0	18.9	907	1632	11.88	26.19	6.03	8.75	445	801	1.95	2.83	6.22	9.02
18	Military	12.6	18.3	889	1601	12.03	26.53	3.75	5.44	554	997	.76	1.10	4.38	6.36
19	Military	13.0	18.9	903	1625	11.86	26.14	5.72	8.30	573	1031	.75	1.08	6.18	8.97
20	Maximum	12.3	17.8	1917	3450	13.07	28.81	3.54	5.13	528	950	1.41	2.04	1.98	2.88
21	A	12.5	18.2	1645	2961	12.82	28.27	2.83	4.10	538	969	.93	1.35	2.00	2.90
22	B	12.7	18.4	1440	2592	12.77	28.15	2.53	3.67	579	1043	.87	1.26	1.98	2.88
23	Military	12.5	18.2	862	1552	11.94	26.32	1.81	2.63	508	915	.75	1.08	1.99	2.88
24	Maximum	12.2	17.7	1922	3460	13.02	28.70	3.50	5.08	529	953	1.36	1.97	4.41	6.40
25	A	12.5	18.1	1664	2995	12.85	28.34	2.86	4.15	551	991	.92	1.33	4.40	6.38
26	B	12.8	18.5	1439	2590	12.63	27.84	2.58	3.74	546	983	.90	1.31	4.40	6.38

<sup>a</sup>Estimated ambient static temperature, 339 K (610° R).

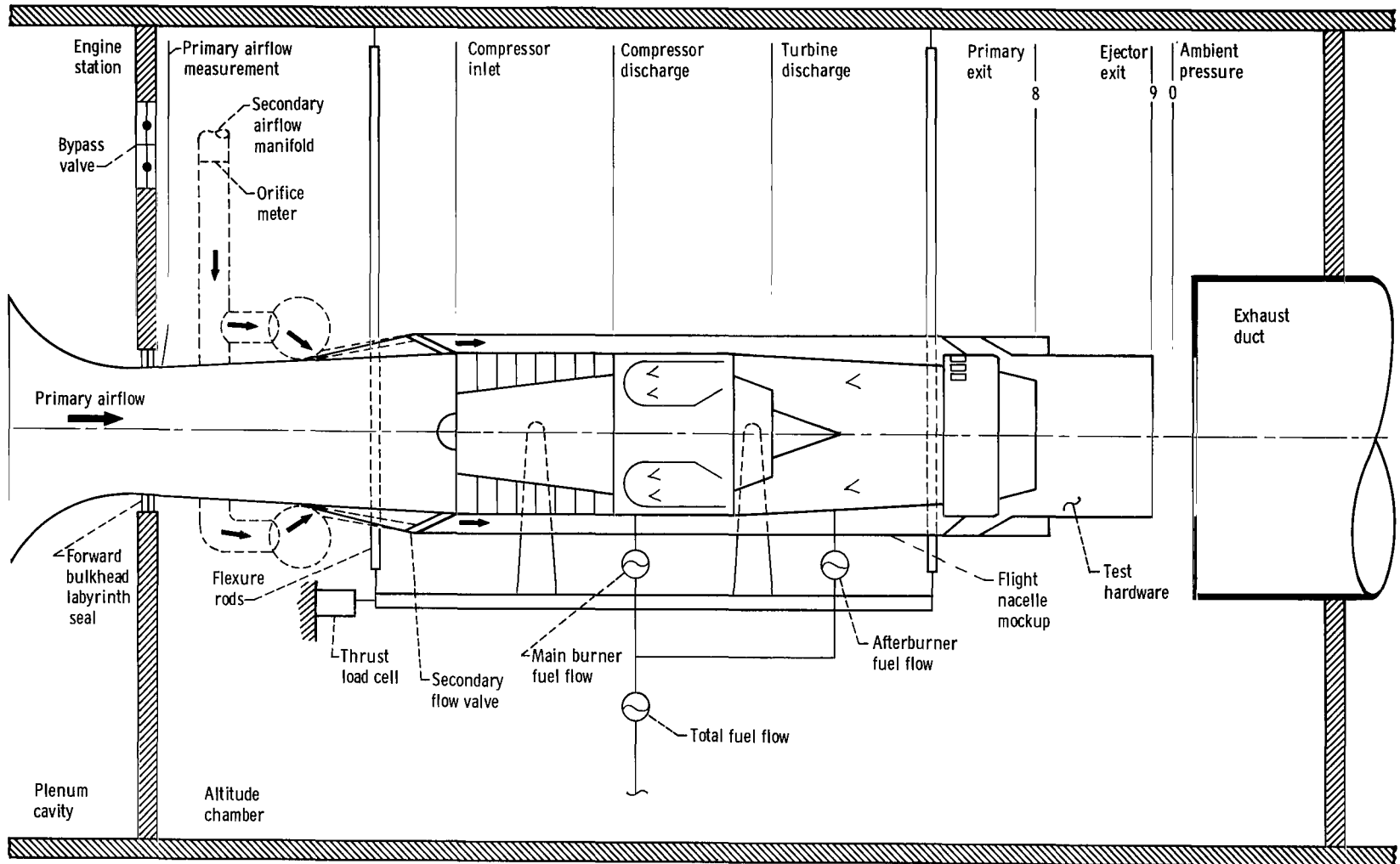
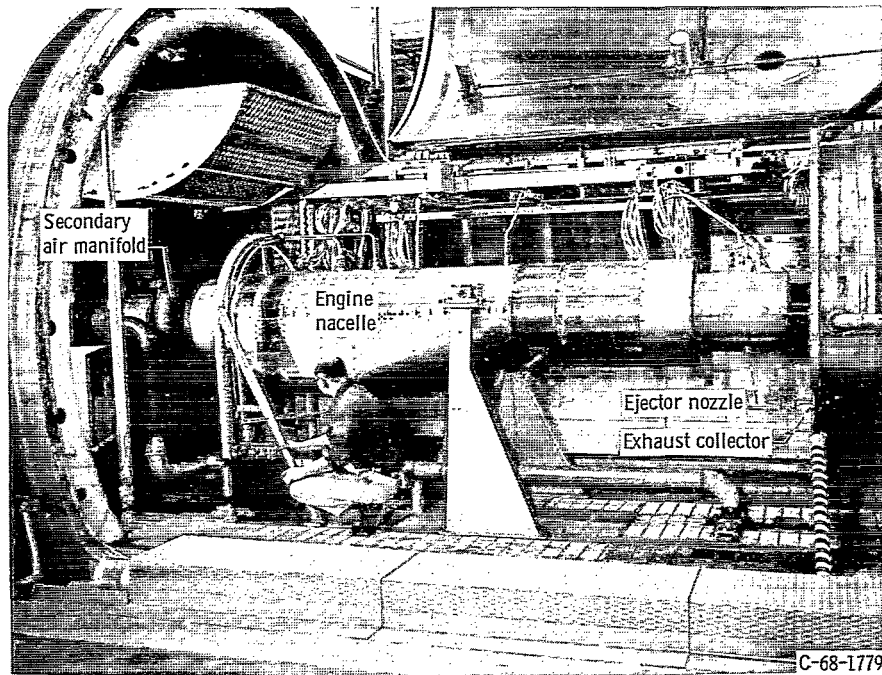


Figure 1. - Schematic of test installation.



C-68-1779

Figure 2. - Test hardware in altitude chamber.

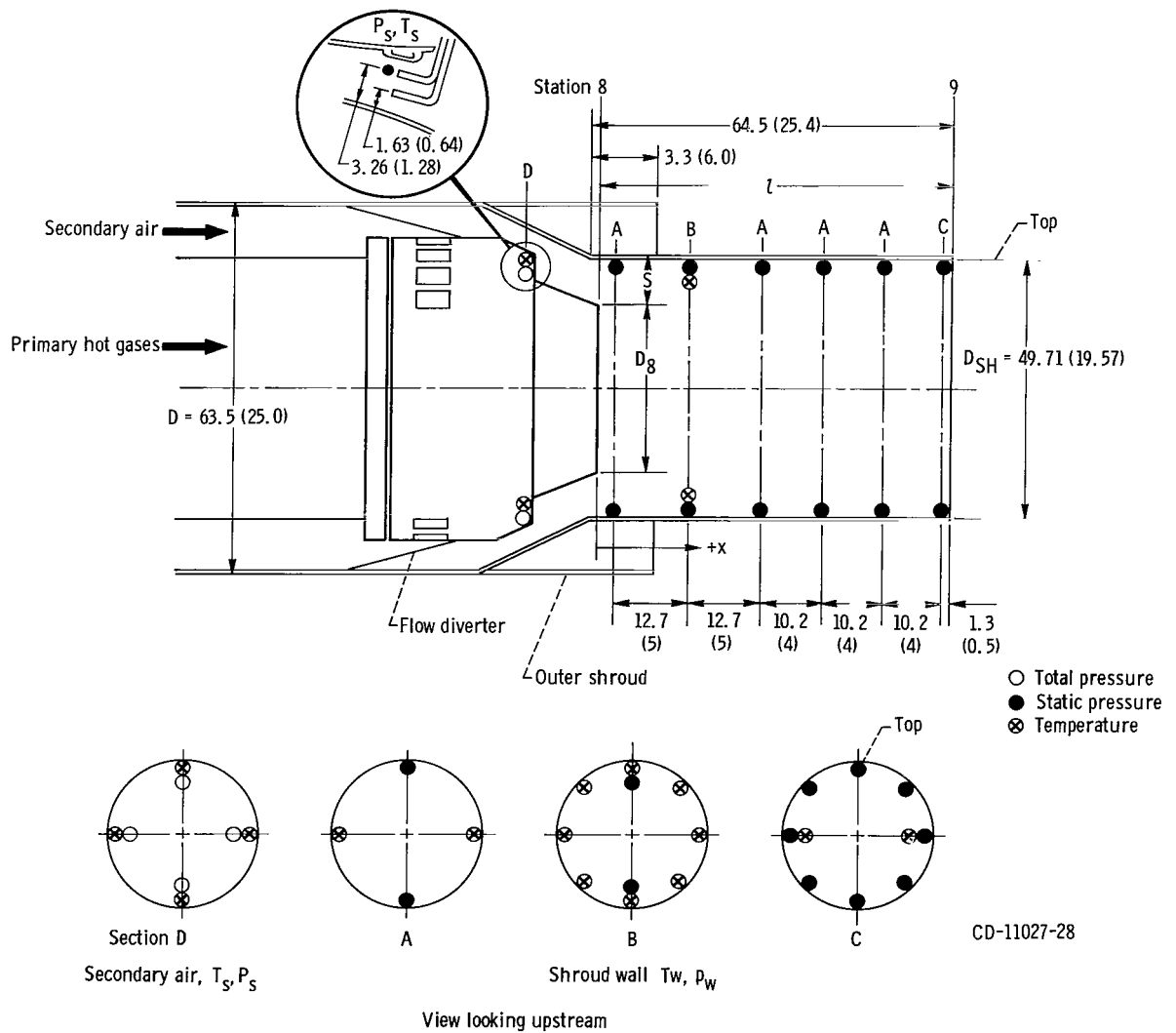


Figure 3. - Ejector geometry and instrumentation. (Dimensions in cm (in.))

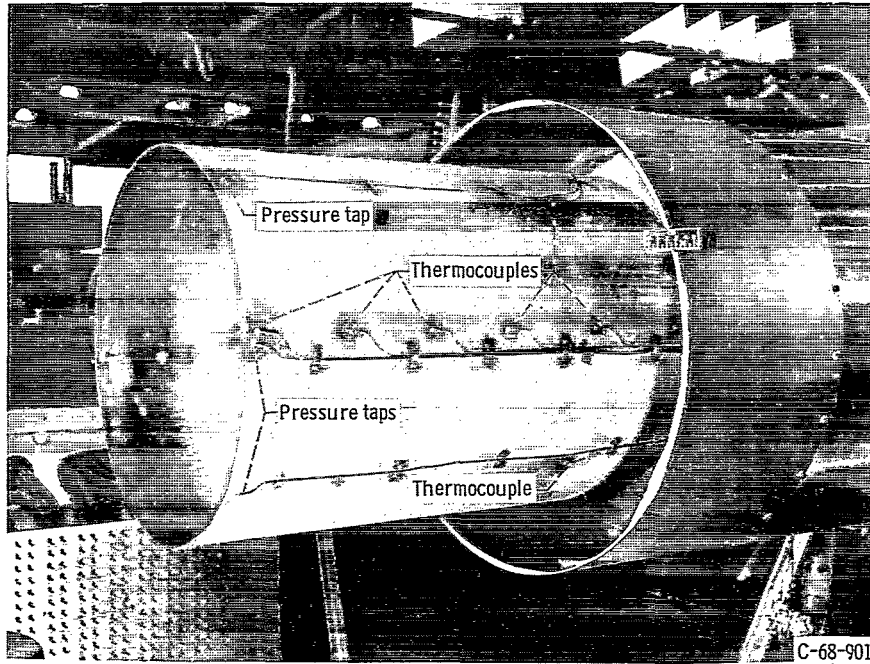


Figure 4. - Typical cylindrical ejector with instrumentation.

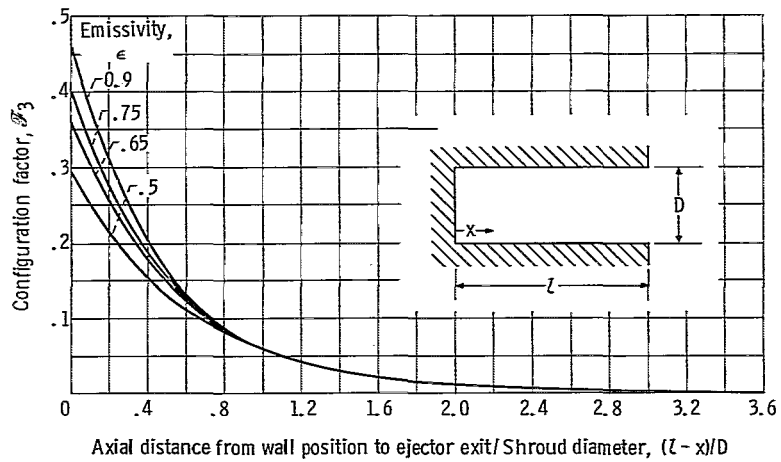
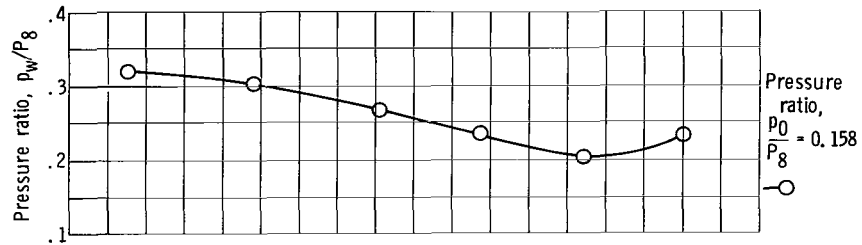
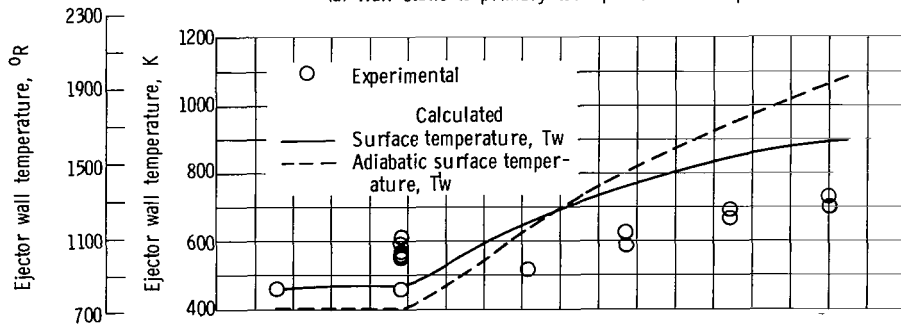


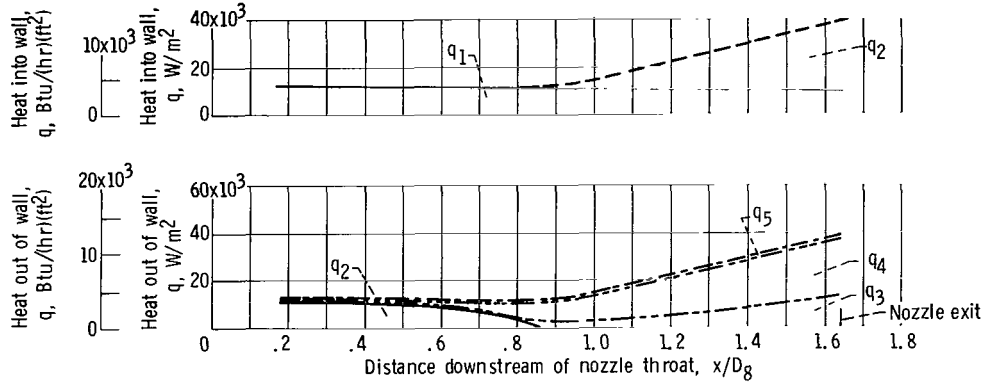
Figure 5. - Inside local wall radiation configuration factor.



(a) Wall static to primary total pressure ratio profile.

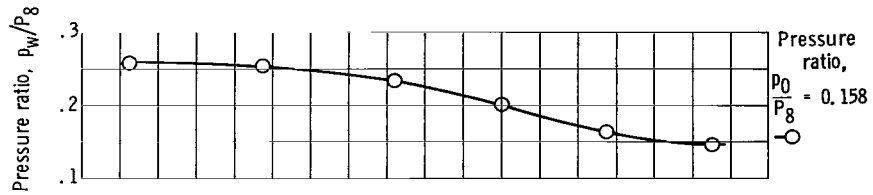


(b) Comparison of experimental and predicted wall temperature profiles.

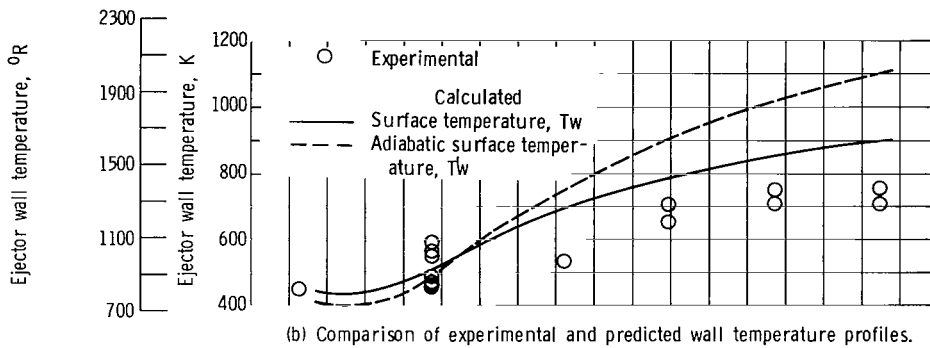


(c) Predicted heat distribution profile.

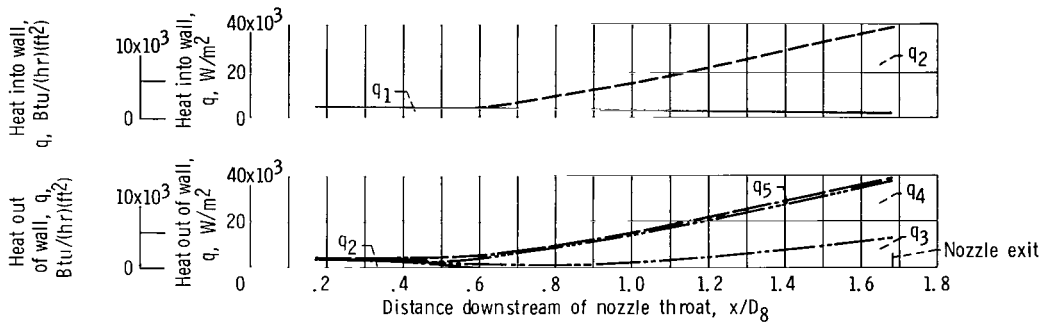
Figure 6. - Comparison of calculated and experimental data for nonimpingement underexpanded flow. Maximum reheat; nozzle pressure ratio  $P_8/P_0$ , 6.3; corrected weight-flow ratio  $\omega\sqrt{\tau}$ , 0.088; secondary to primary total-pressure ratio  $P_s/P_8$ , 0.407; primary total temperature  $T_p$ , 1924 K (3464° R).



(a) Wall static to primary total pressure ratio profile.

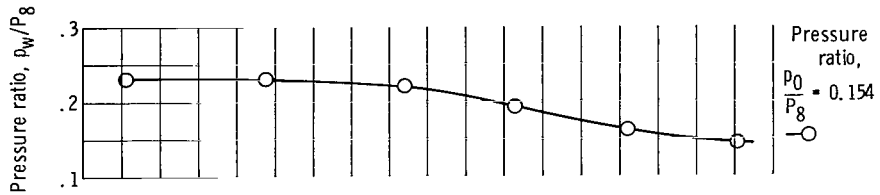


(b) Comparison of experimental and predicted wall temperature profiles.

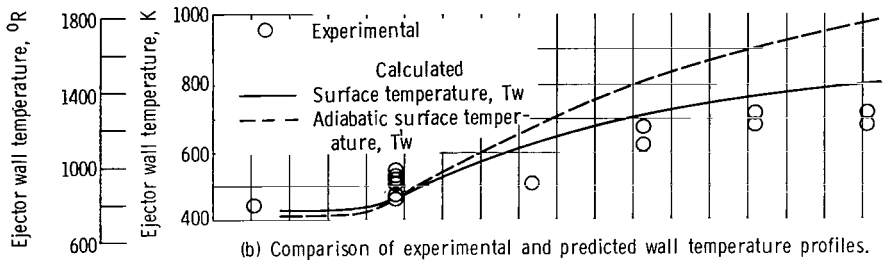


(c) Predicted heat distribution profile.

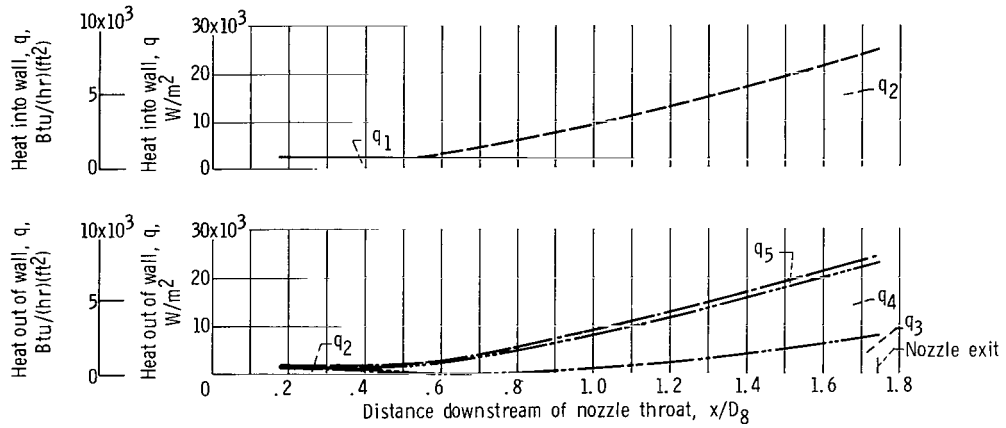
Figure 7. - Comparison of calculated and experimental data for nonimpingement underexpanded flow. Reheat A; nozzle pressure ratio  $P_8/P_0$ , 6.3; corrected weight-flow ratio  $\omega\sqrt{\tau}$ , 0.067; secondary to primary total-pressure ratio  $P_5/P_8$ , 0.312; primary total temperature  $T_p$ , 1639 K (2950° R).



(a) Wall static to primary total pressure ratio profile.



(b) Comparison of experimental and predicted wall temperature profiles.



(c) Predicted heat distribution profile.

Figure 8. - Comparison of calculated and experimental data for nonimpingement underexpanded flow. Reheat B; nozzle pressure ratio  $P_8/P_0$ , 6.5; corrected weight-flow ratio  $\omega\sqrt{T}$ , 0.069; secondary to primary total-pressure ratio  $P_5/P_8$ , 0.279; primary total temperature  $T_p$ , 1434 K (2582° R).

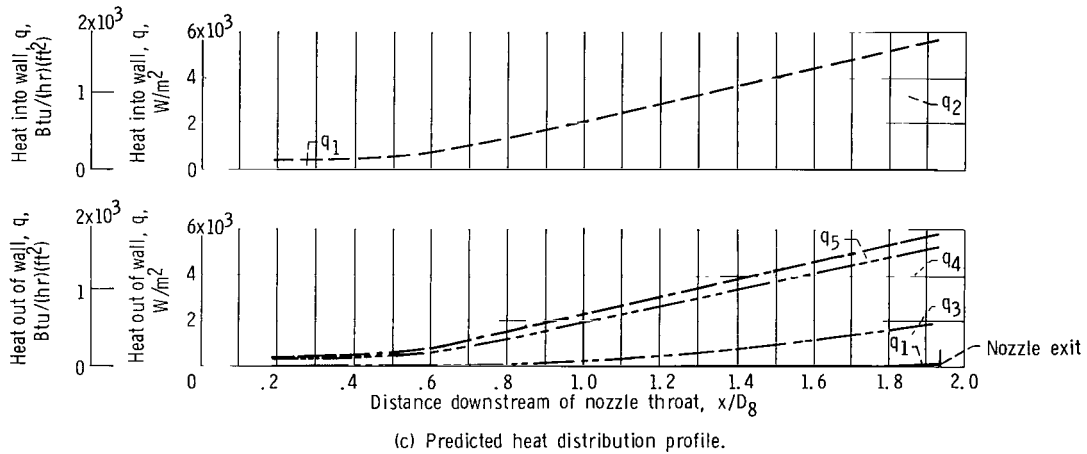
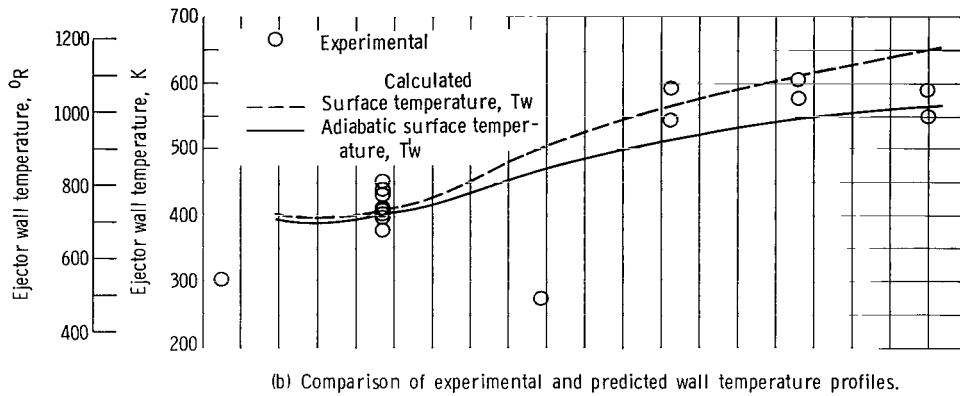
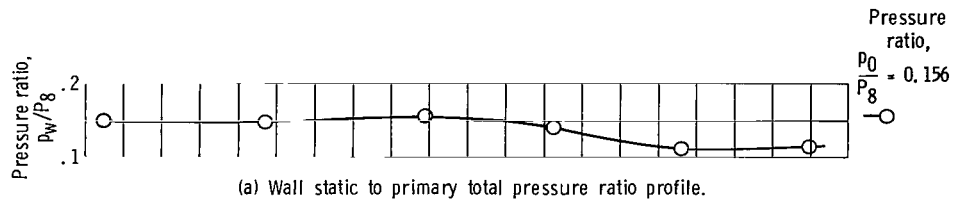


Figure 9. - Comparison of calculated and experimental data for nonimpingement underexpanded flow. Military setting; nozzle pressure ratio  $P_8/p_0$ , 6.4; corrected weight-flow ratio  $\omega\sqrt{\tau}$ , 0.073; secondary to primary total-pressure ratio  $P_5/P_8$ , 0.204; primary total temperature  $T_p$ , 881 K (1585° R).

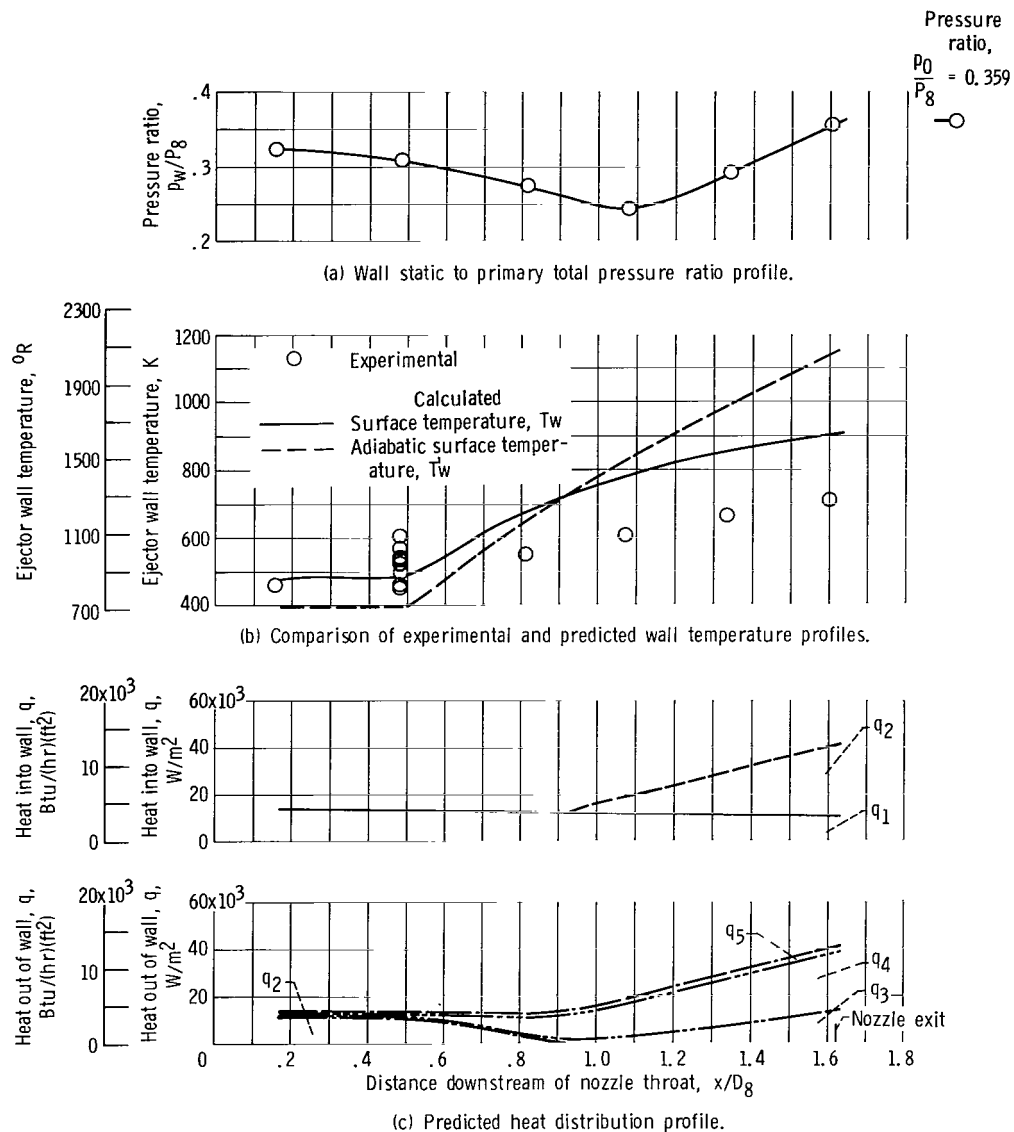


Figure 10. - Comparison of calculated and experimental data for nonimpingement overexpanded flow. Maximum reheat; nozzle pressure ratio  $P_8/p_0$ , 2.8; corrected weight-flow ratio  $\omega\sqrt{\tau}$ , 0.087; secondary to primary total-pressure ratio  $P_5/P_8$ , 0.415; primary total temperature  $T_p$ , 1933 K (3480° R).

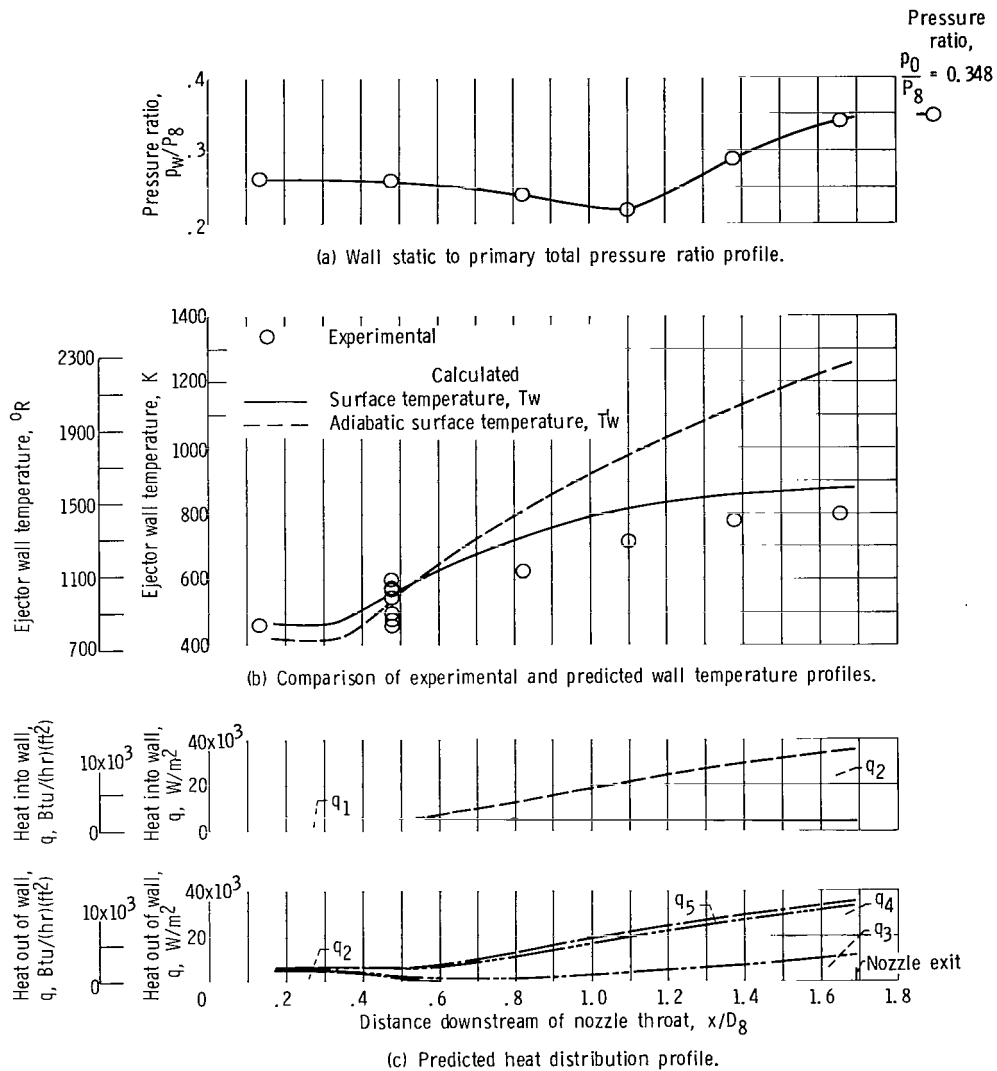
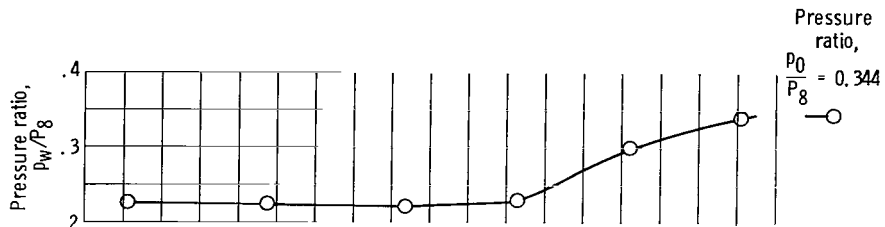
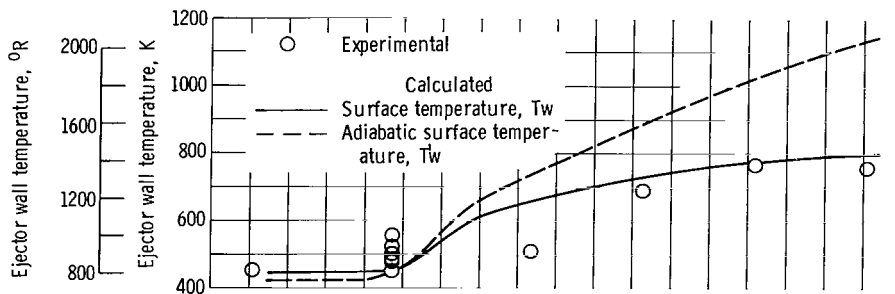


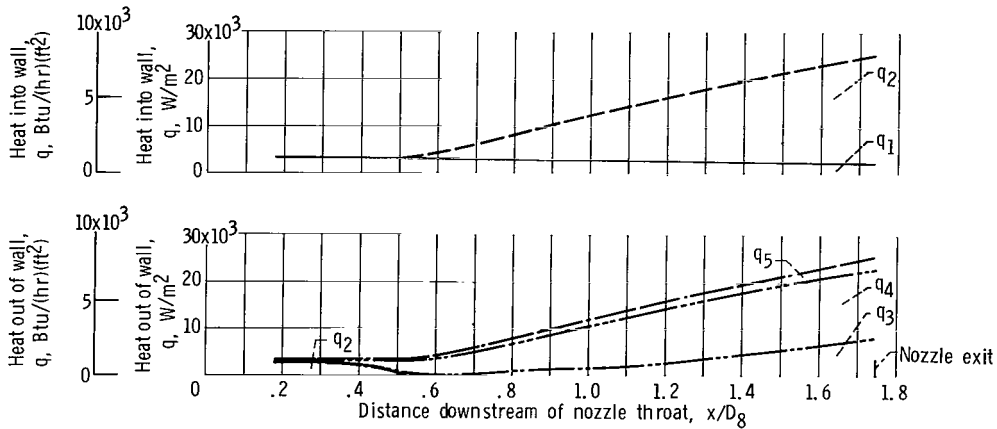
Figure 11. - Comparison of calculated and experimental data for nonimpingement overexpanded flow. Reheat A; nozzle pressure ratio  $P_8/p_0$ , 2.9; corrected weight-flow ratio  $\omega\sqrt{\tau}$ , 0.063; secondary to primary total-pressure ratio  $P_5/P_8$ , 0.313; primary total temperature  $T_p$ , 1674 K (3013° R).



(a) Wall static to primary total pressure ratio profile.



(b) Comparison of experimental and predicted wall temperature profiles.



(c) Predicted heat distribution profile.

Figure 12. - Comparison of calculated and experimental data for nonimpingement overexpanded flow. Reheat B; nozzle pressure ratio  $P_8/P_0$ , 2.9; corrected weight-flow ratio  $\omega\sqrt{\tau}$ , 0.059; secondary to primary total-pressure ratio  $P_5/P_8$ , 0.276; primary total temperature  $T_p$ , 1451 K (2612° R).

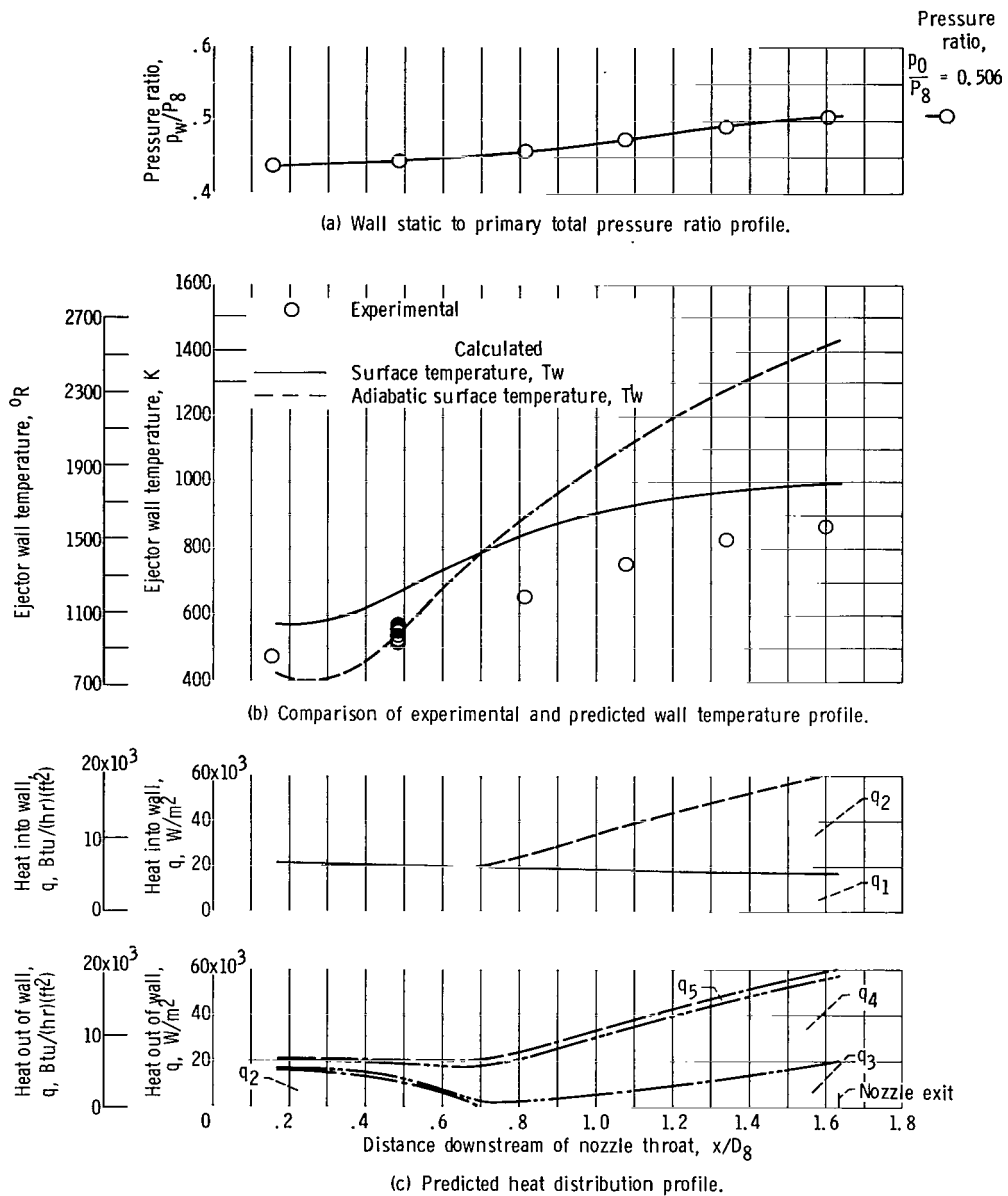
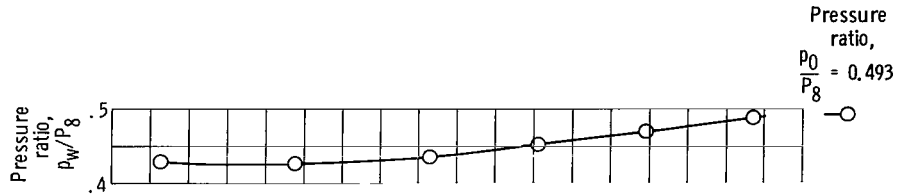
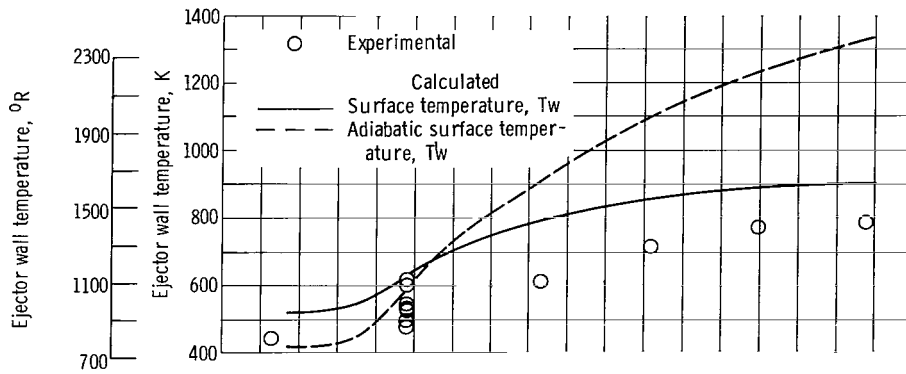


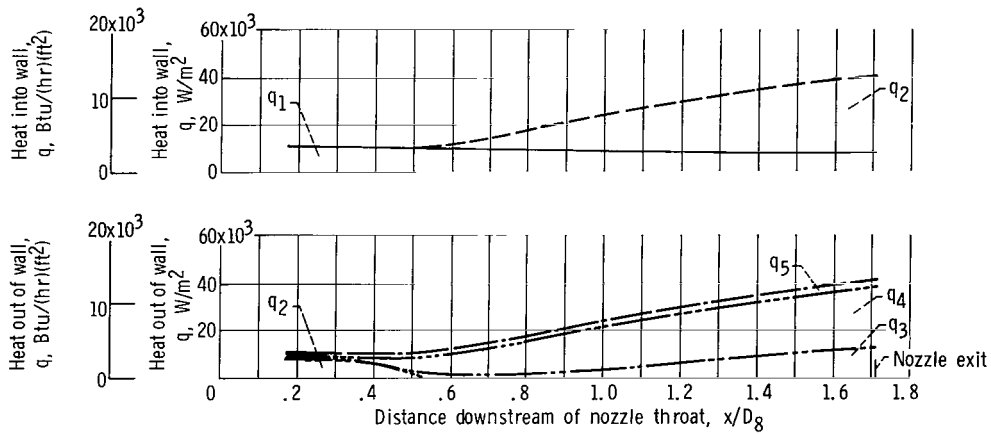
Figure 13. - Comparison of calculated and experimental data for unattached flow. Maximum reheat; nozzle pressure ratio  $P_8/P_0$ , 2.0; corrected weight-flow ratio  $\omega\sqrt{\tau}$ , 0.074; secondary to primary total-pressure ratio  $P_5/P_8$ , 0.481; primary total temperature  $T_p$ , 1940 K (3492° R).



(a) Wall static to primary total pressure ratio profile.



(b) Comparison of experimental and predicted wall temperature profiles.



(c) Predicted heat distribution profile.

Figure 14. - Comparison of calculated and experimental data for unattached flow. Reheat A; nozzle pressure ratio  $P_8/P_0$ , 2.0; corrected weight-flow ratio  $\omega\sqrt{T}$ , 0.067; secondary to primary total-pressure ratio  $P_5/P_8$ , 0.453; primary total temperature  $T_p$ , 1634 K (2941° R).

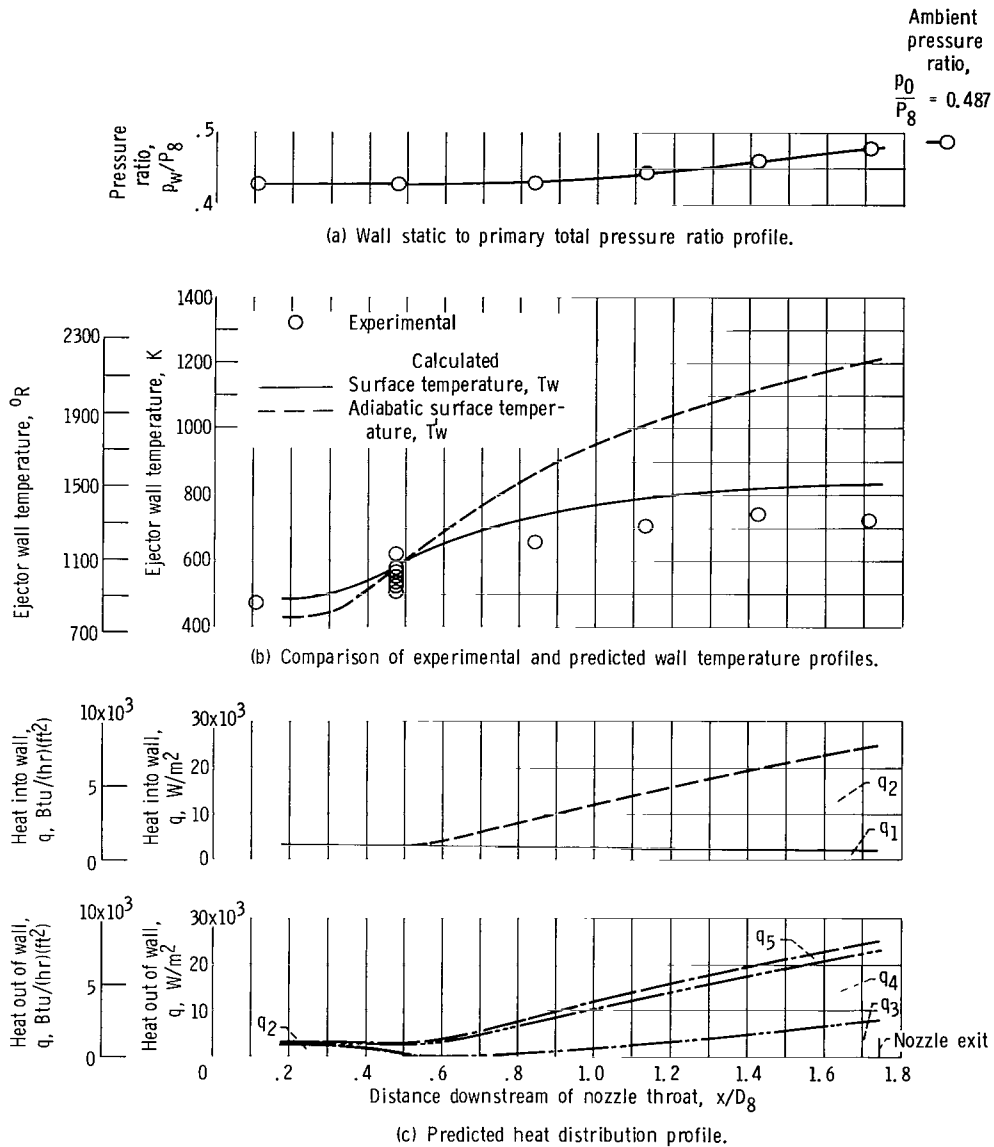


Figure 15. - Comparison of calculated and experimental data for unattached flow. Reheat B; nozzle pressure ratio  $P_8/p_0$ , 2.1; corrected weight-flow ratio  $\omega\sqrt{\tau}$ , 0.068; secondary to primary total-pressure ratio  $P_5/P_8$ , 0.453; primary total temperature  $T_p$ , 1438 K (2589° R).

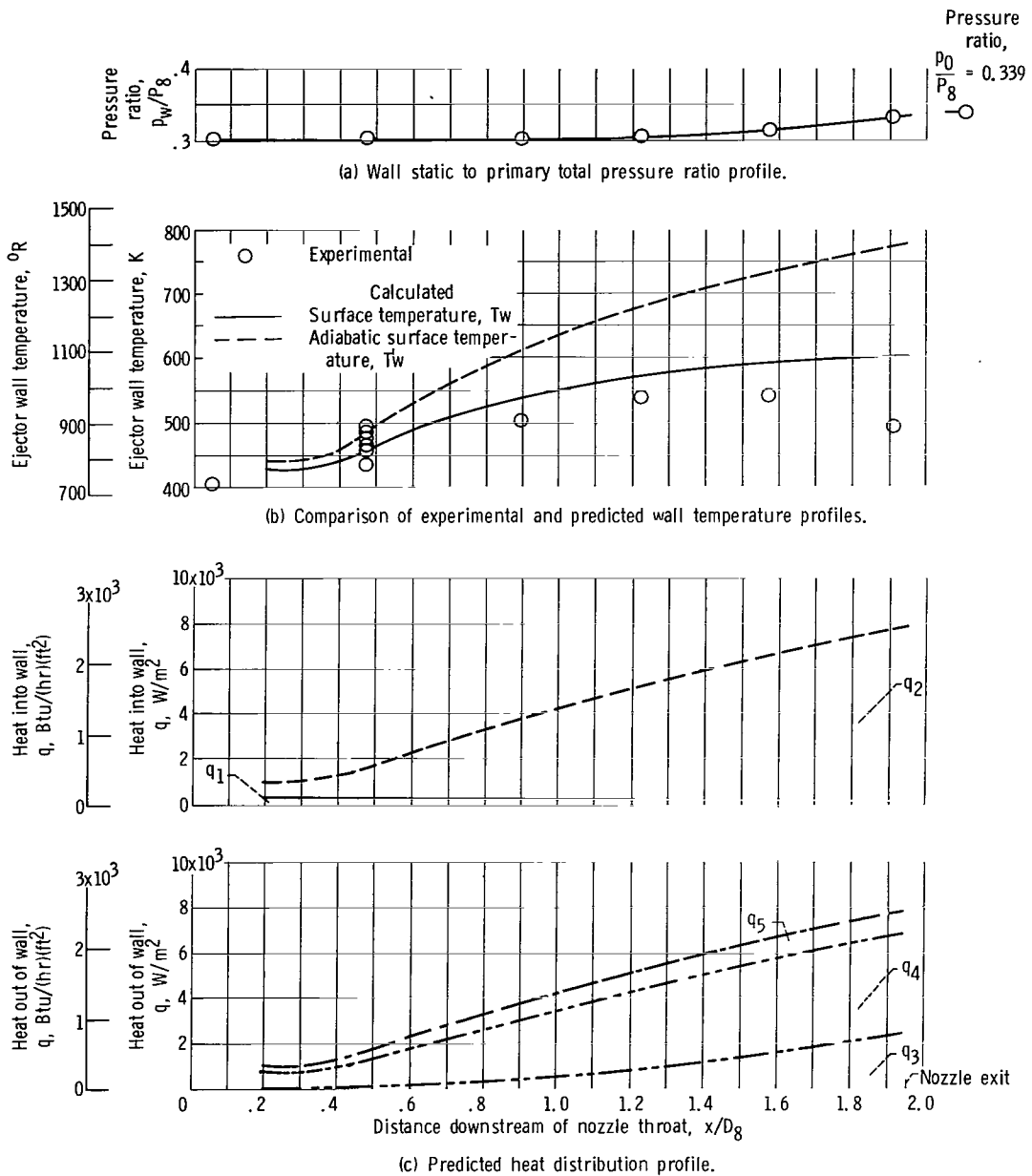


Figure 16. - Comparison of calculated and experimental data for unattached flow. Military setting; nozzle pressure ratio  $P_8/P_0$ , 3.0; corrected weight-flow ratio  $\omega\sqrt{\tau}$ , 0.078; secondary to primary total-pressure ratio  $P_5/P_8$ , 0.329; primary total temperature  $T_p$ , 895 K (1611° R).

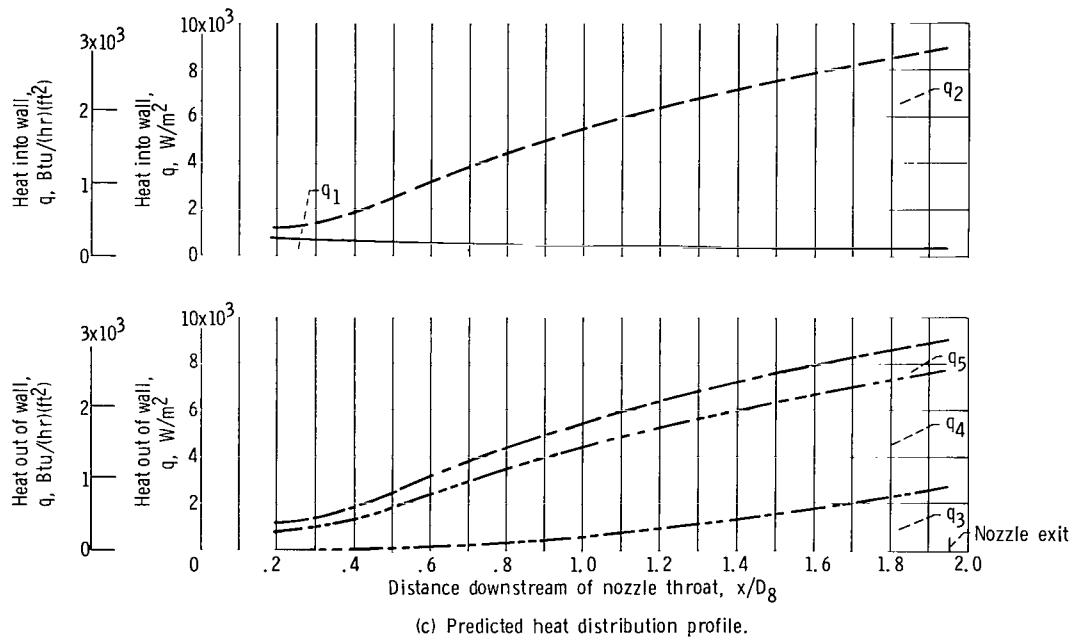
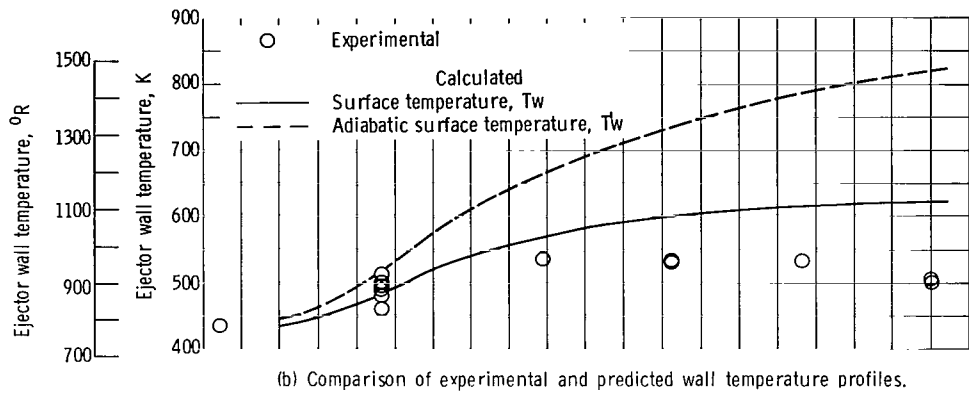
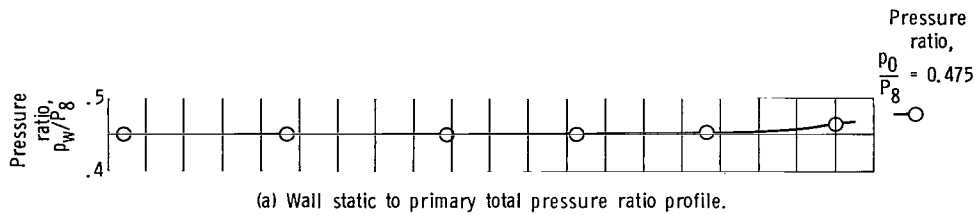
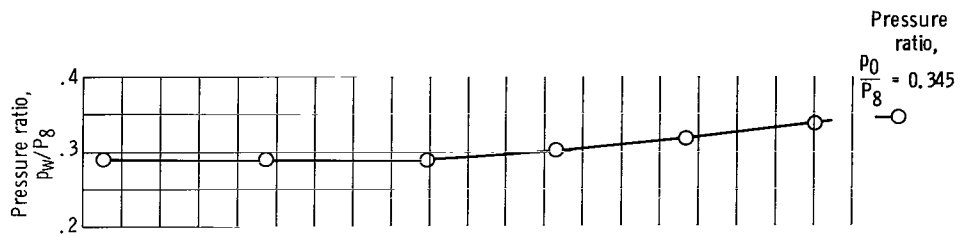
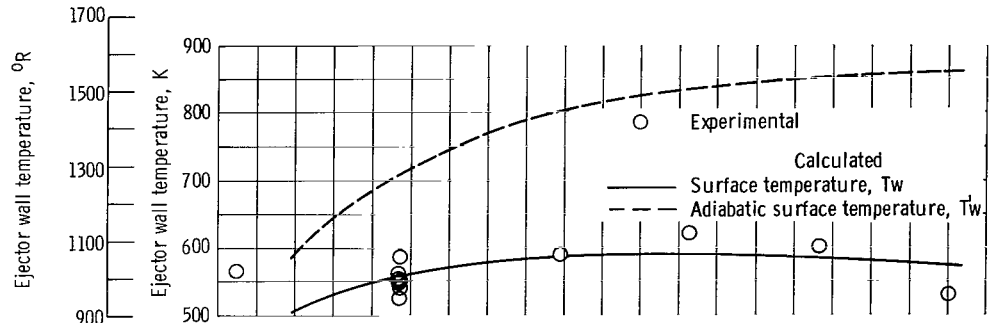


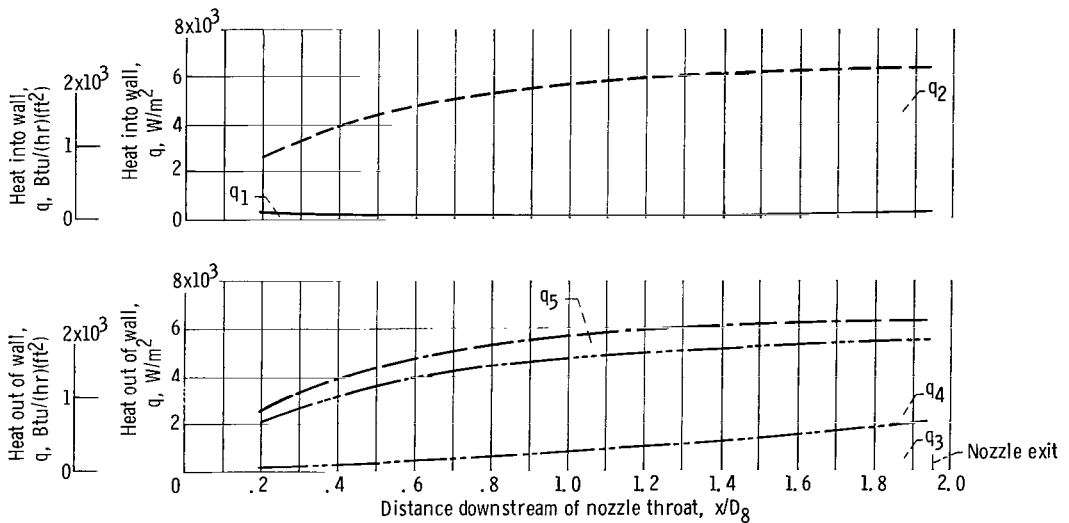
Figure 17. - Comparison of calculated and experimental data for unattached flow. Military setting; nozzle pressure ratio  $P_8/P_0$ , 2.1; corrected weight-flow ratio  $\omega\sqrt{T}$ , 0.076; secondary to primary total-pressure ratio  $P_5/P_8$ , 0.464; primary total temperature  $T_p$ , 907 K (1632° R).



(a) Wall static to primary total pressure ratio profile.



(b) Comparison of experimental and predicted wall temperature profiles.



(c) Predicted heat distribution profile.

Figure 18. - Comparison of calculated and experimental data for unattached flow. Military setting; nozzle pressure ratio  $P_8/P_0$ , 2.9; corrected weight-flow ratio  $\omega\sqrt{T}$ , 0.033; secondary to primary total-pressure ratio  $P_5/P_8$ , 0.297; primary total temperature  $T_p$ , 889 K (1601° R).

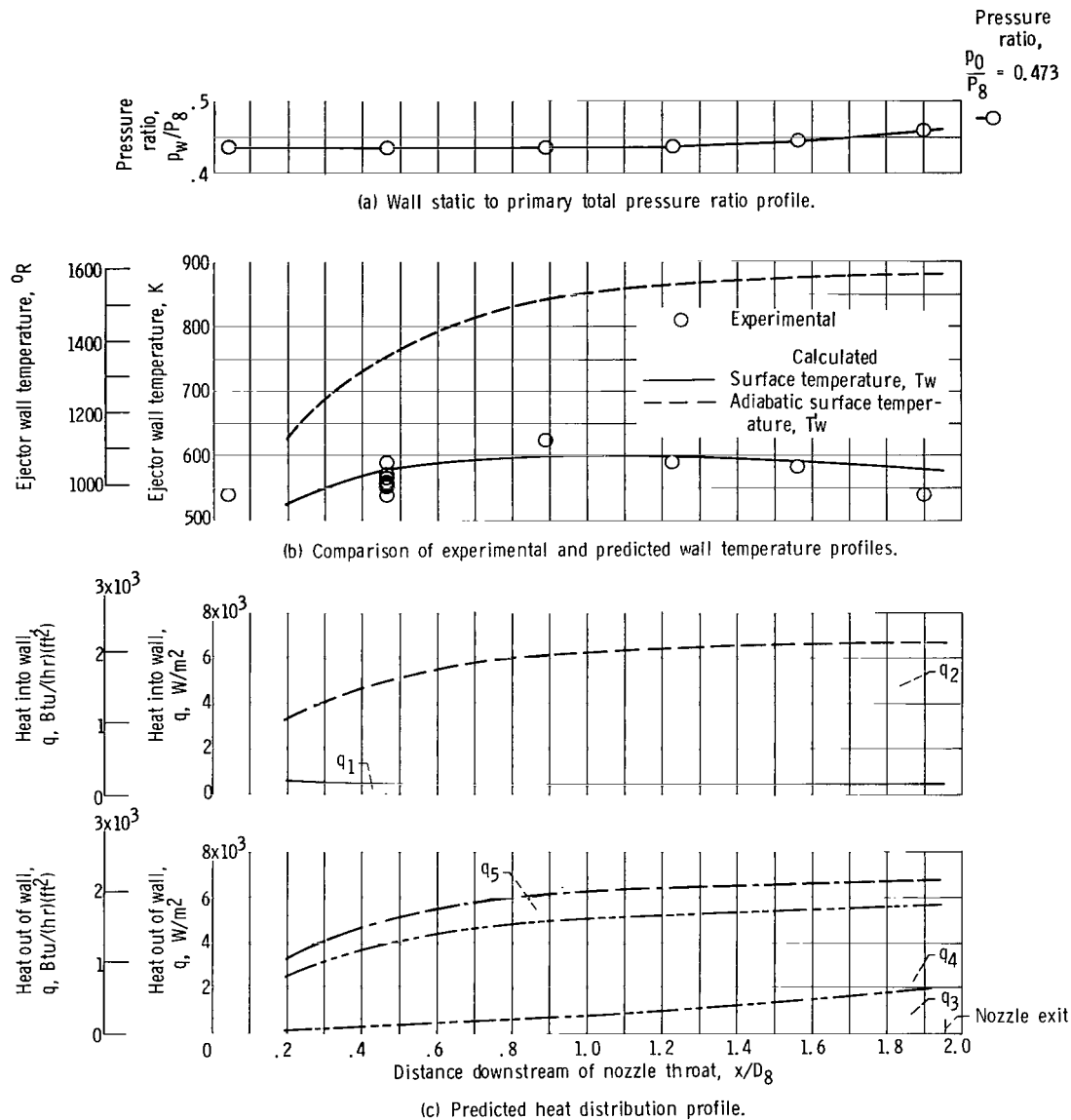
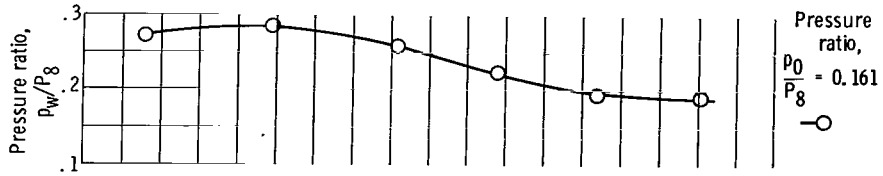
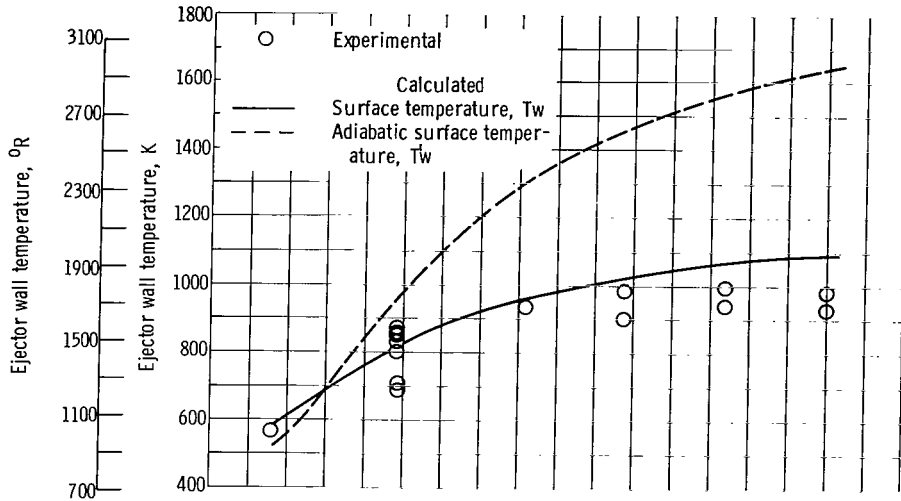


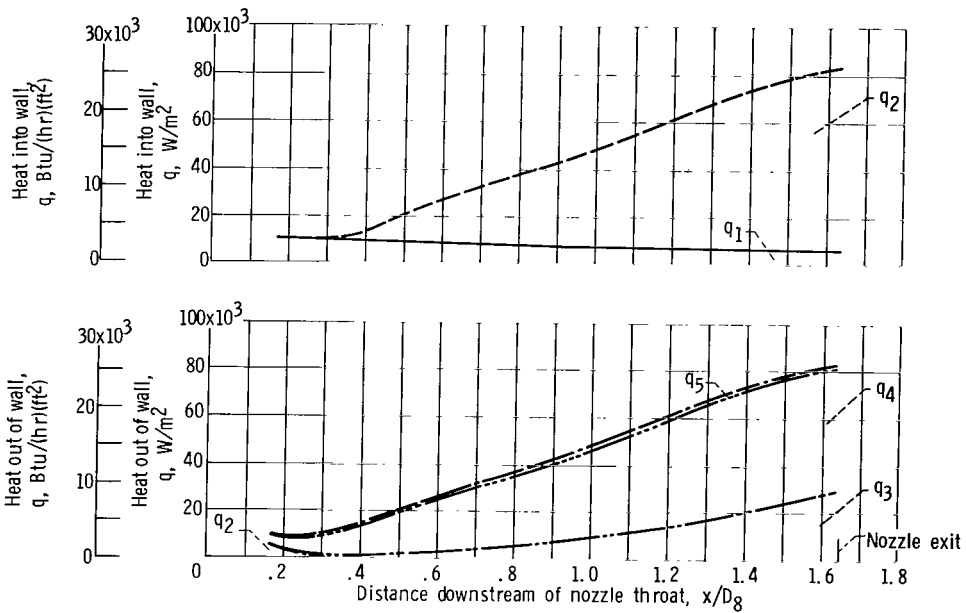
Figure 19. - Comparison of calculated and experimental data for unattached flow. Military setting; nozzle pressure ratio  $P_8/p_0$ , 2.1; corrected weight-flow ratio  $\omega\sqrt{T}$ , 0.033; secondary to primary total-pressure ratio  $P_5/P_8$ , 0.439; primary total temperature  $T_p$ , 903 K (1625° R).



(a) Wall static to primary total pressure ratio profile.

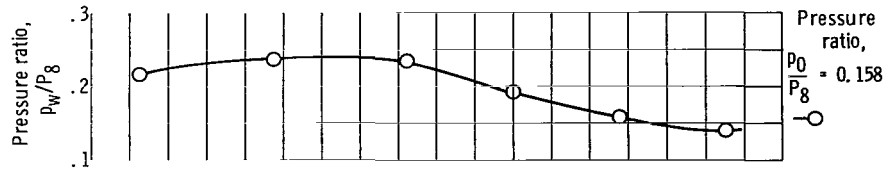


(b) Comparison of experimental and predicted wall temperature profile.

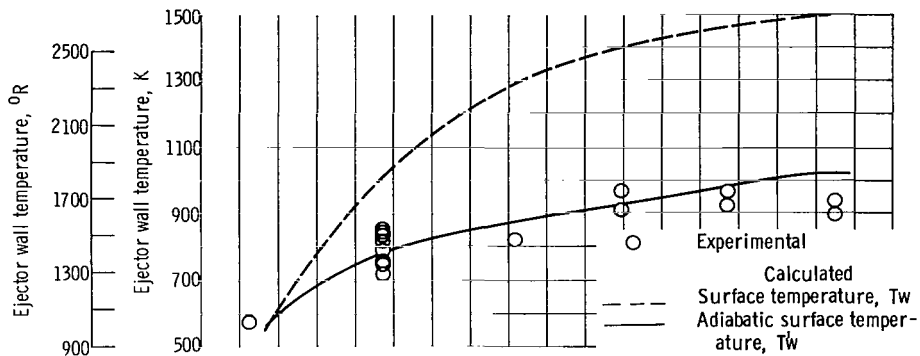


(c) Predicted heat distribution profile.

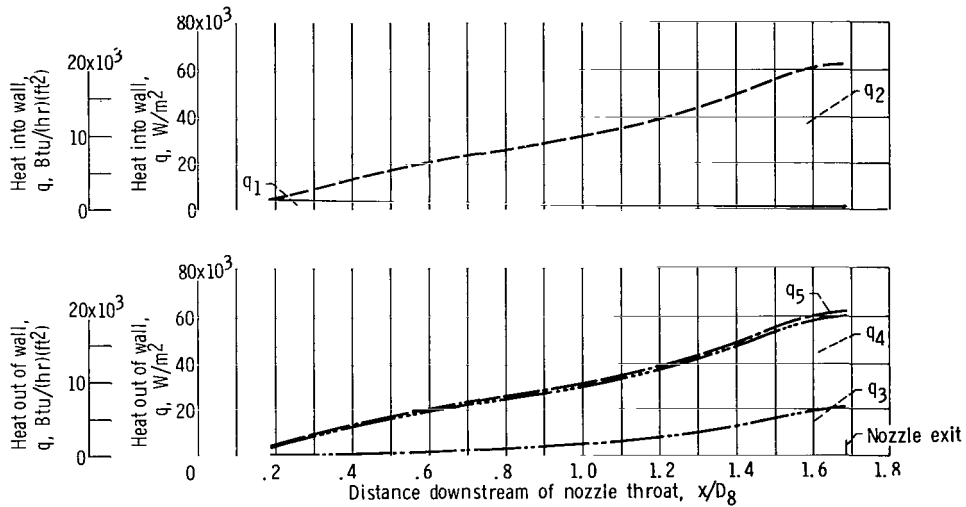
Figure 20. - Comparison of calculated and experimental data for impingement underexpanded flow. Maximum reheat; nozzle pressure ratio  $P_8/p_0$ , 6.2; corrected weight-flow ratio  $\omega\sqrt{T}$ , 0.037; secondary to primary total-pressure ratio  $P_s/P_8$ , 0.289; primary total temperature  $T_p$ , 1917 K (3450° R).



(a) Wall static to primary total pressure ratio profile.

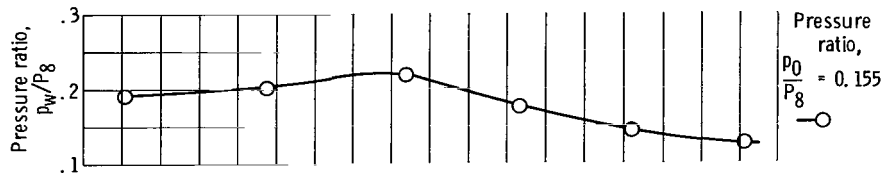


(b) Comparison of experimental and predicted wall temperature profile.

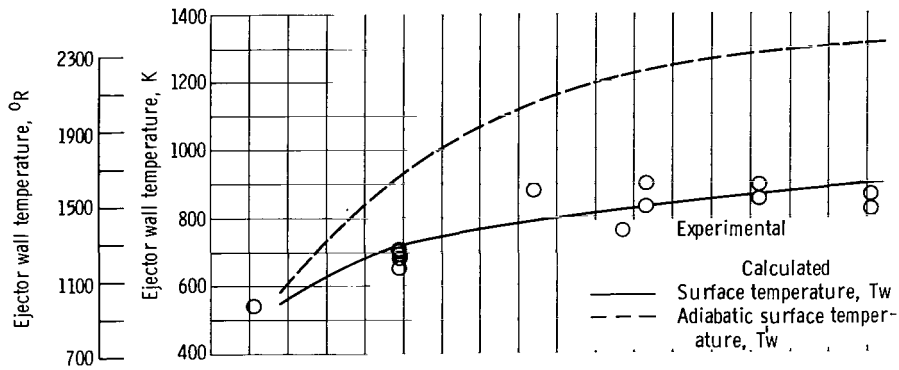


(c) Predicted heat distribution profile.

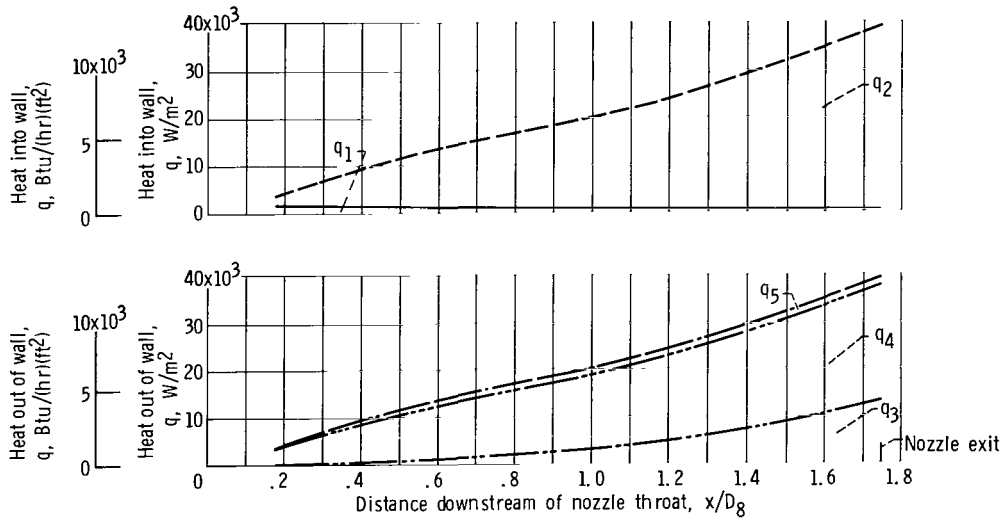
Figure 21. - Comparison of calculated and experimental data for impingement underexpanded flow. Reheat A; nozzle pressure ratio  $P_8/p_0$ , 6.3; corrected weight-flow ratio  $\omega\sqrt{T}$ , 0.027; secondary to primary total-pressure ratio  $P_5/P_8$ , 0.225; primary total temperature  $T_p$ , 1645 K (2961° R).



(a) Wall static to primary total pressure ratio profile.



(b) Comparison of experimental and predicted wall temperature profile.



(c) Predicted heat distribution profile.

Figure 22. - Comparison of calculated and experimental data for impingement underexpanded flow. Reheat B; nozzle pressure ratio  $P_8/p_0$ , 6.4; corrected weight-flow ratio  $\omega\sqrt{\tau}$ , 0.028; secondary to primary total-pressure ratio  $P_5/P_8$ , 0.199; primary total temperature  $T_p$ , 1440 K (2592° R).

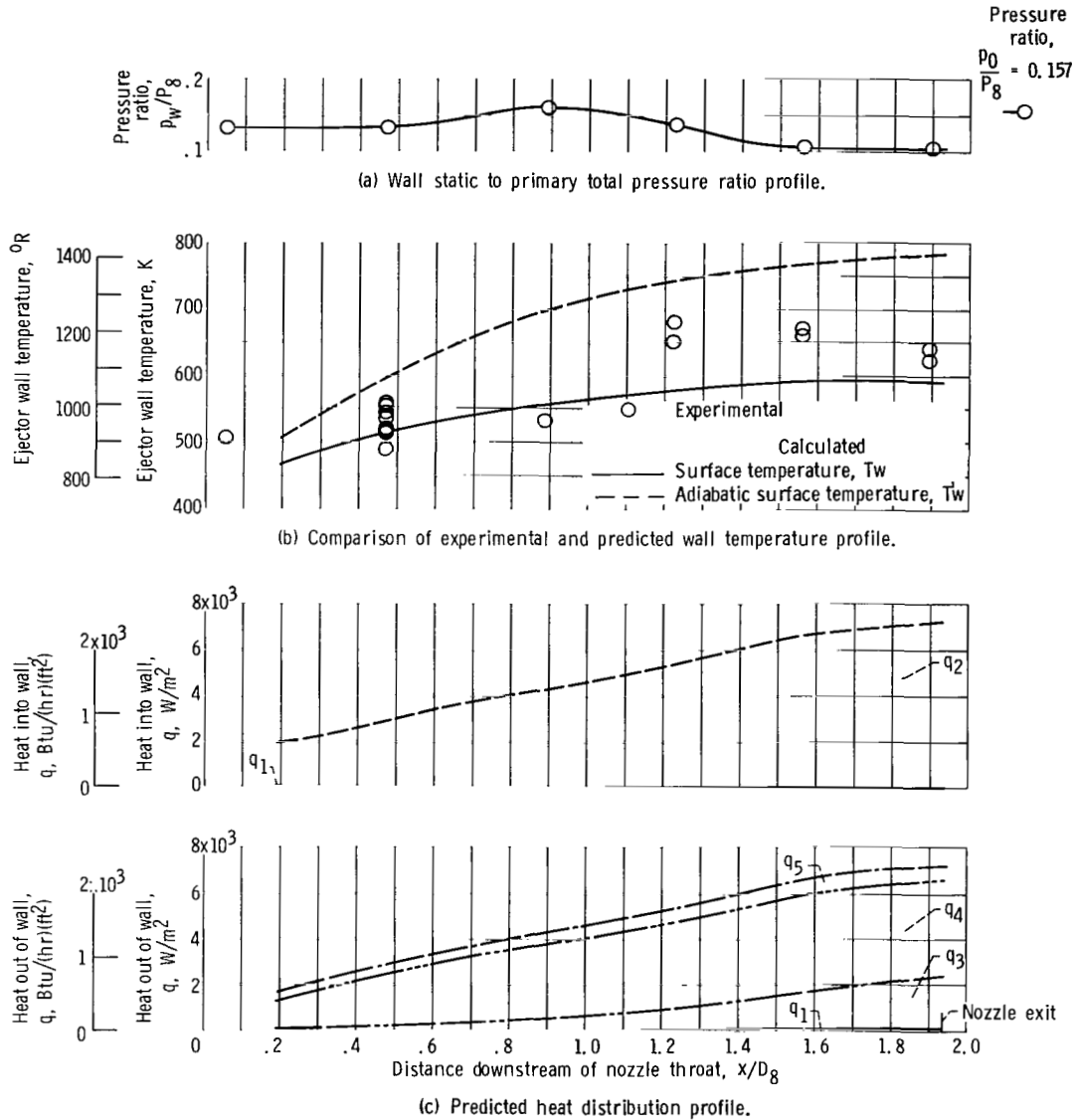


Figure 23. - Comparison of calculated and experimental data for impingement underexpanded flow. Military setting; nozzle pressure ratio  $P_8/p_0$ , 6.4; corrected weight-flow ratio  $\omega\sqrt{T_p}$ , 0.032; secondary to primary total-pressure ratio  $P_5/P_8$ , 0.144; primary total temperature  $T_p$ , 862 K (1552 $^{\circ}$  R).

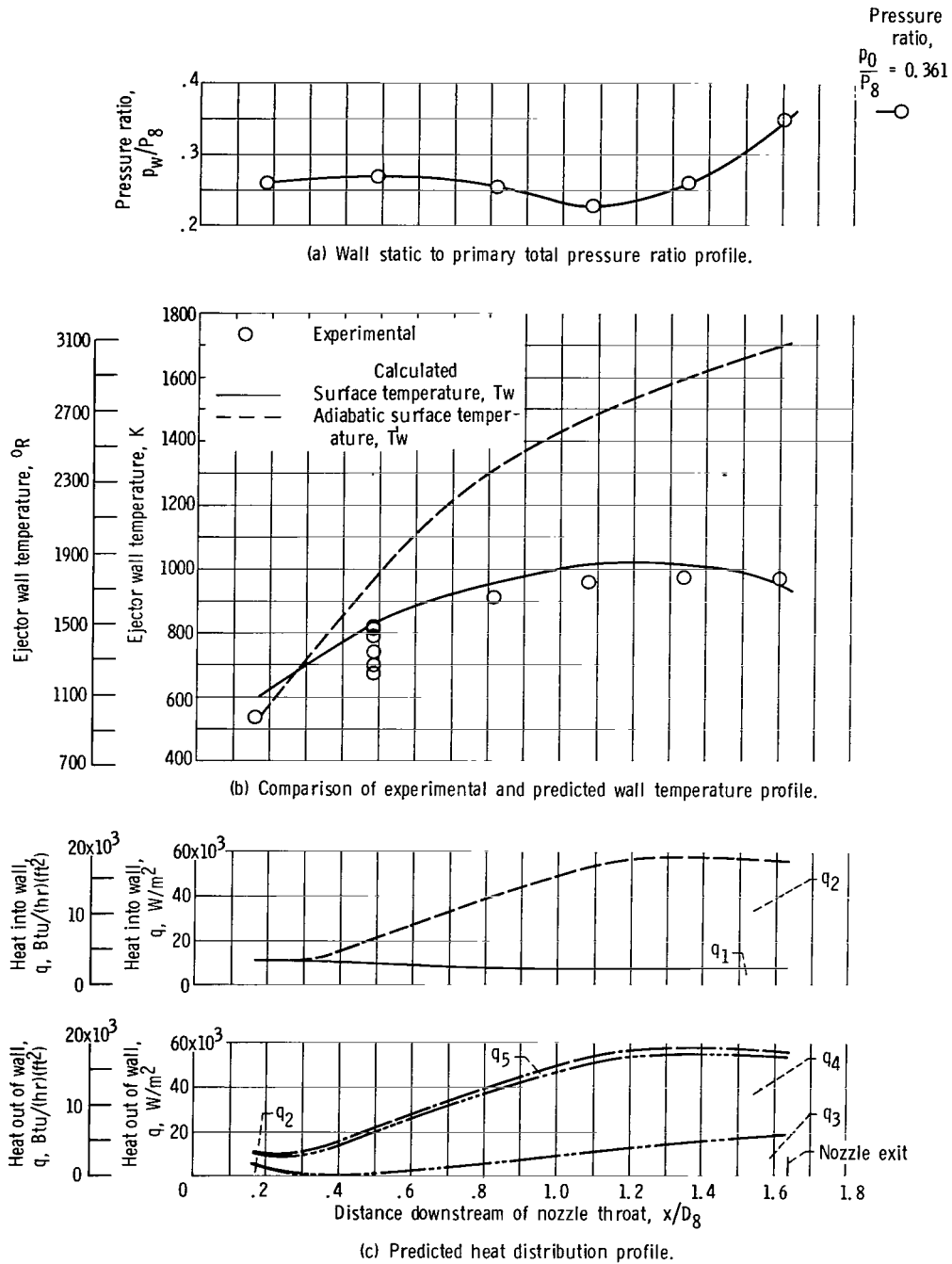
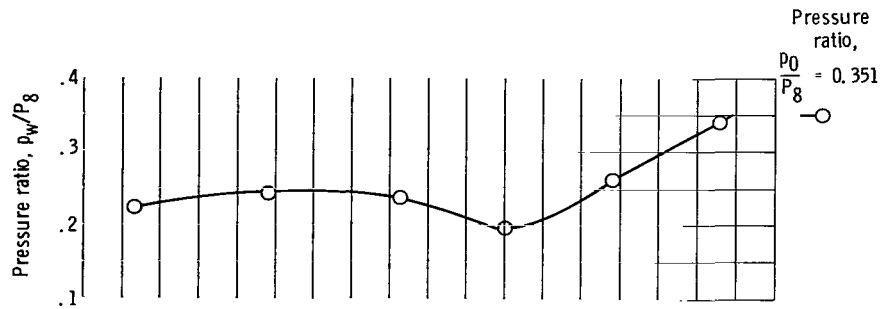
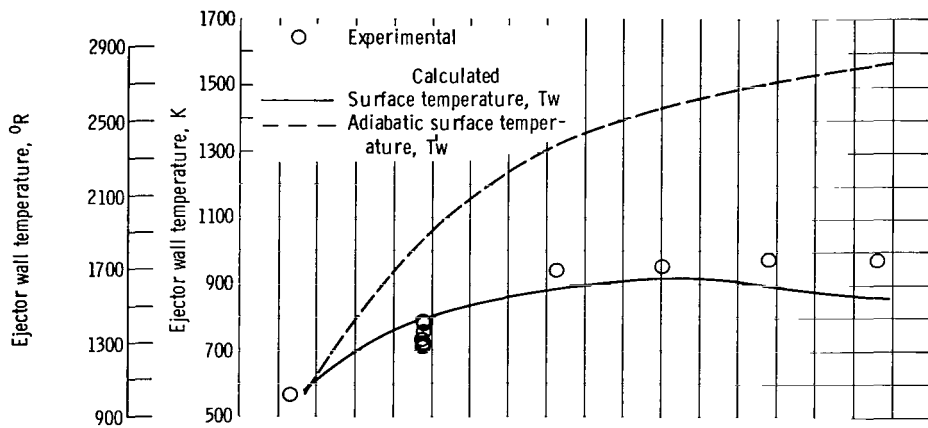


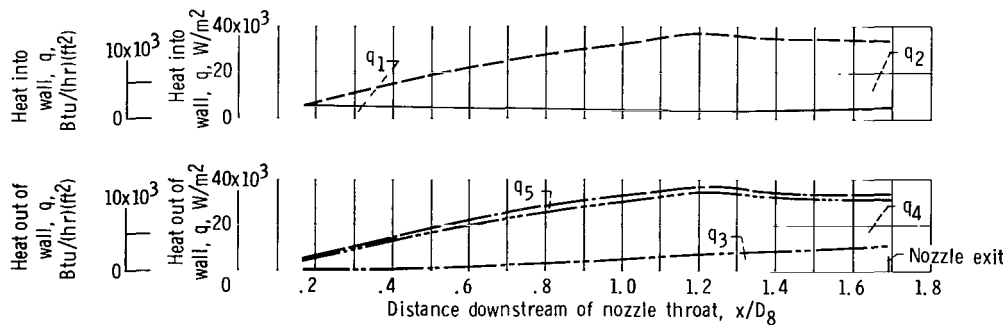
Figure 24. - Comparison of calculated and experimental data for impingement overexpanded flow. Maximum reheat; nozzle pressure ratio  $P_8/p_0$ , 2.8; corrected weight-flow ratio  $\omega\sqrt{\tau}$ , 0.036; secondary to primary total-pressure ratio  $P_5/P_8$ , 0.287; primary total pressure  $T_p$ , 1922 K ( $3460^\circ R$ ).



(a) Wall static to primary total pressure ratio profile.

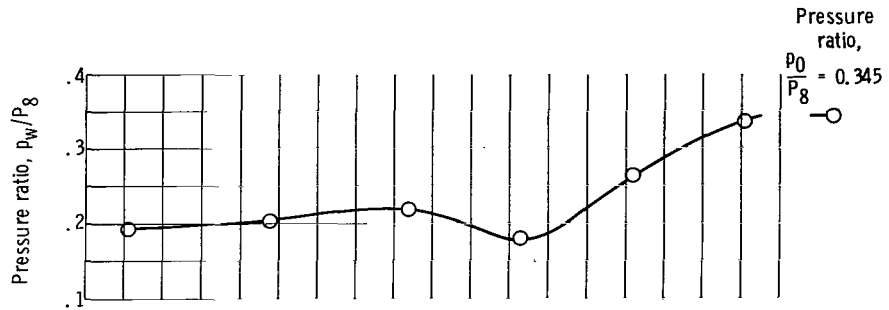


(b) Comparison of experimental and predicted wall temperature profiles.

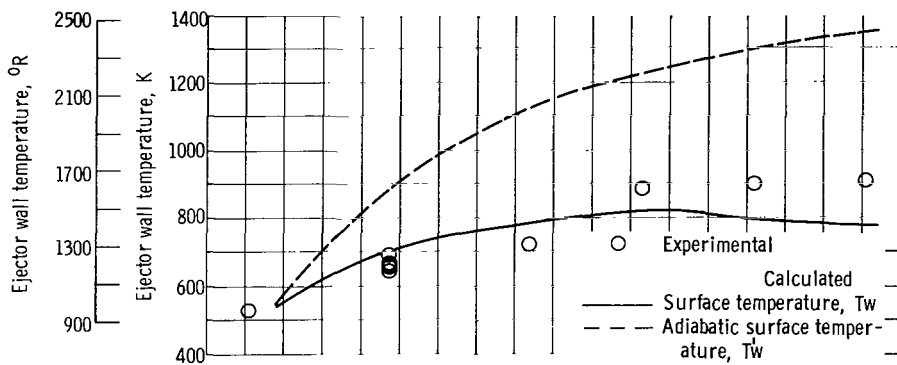


(c) Predicted heat distribution profile.

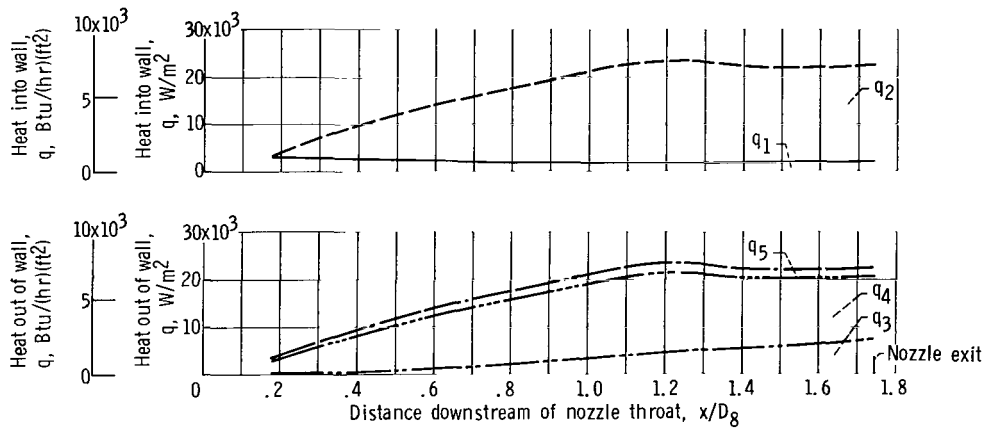
Figure 25. - Comparison of calculated and experimental data for impingement overexpanded flow. Reheat A; nozzle pressure ratio  $P_8/P_0$ , 2.8; corrected weight-flow ratio  $\omega\sqrt{\tau}$ , 0.027; secondary to primary total-pressure ratio  $P_5/P_8$ , 0.229; primary total temperature  $T_p$ , 1664 K (2995° R).



(a) Wall static to primary total pressure ratio profile.

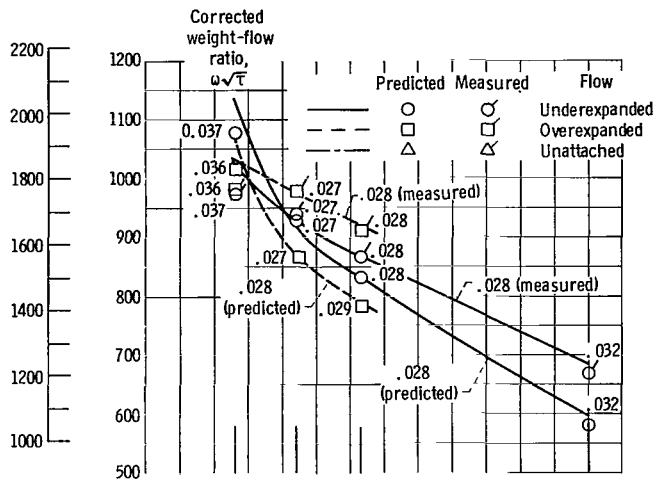


(b) Comparison of experimental and predicted wall temperature profiles.

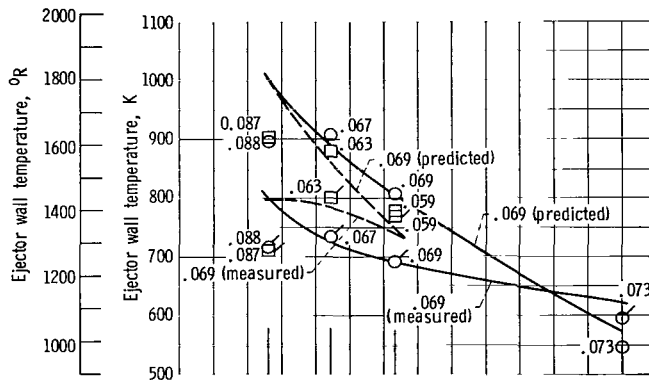


(c) Predicted heat distribution profile.

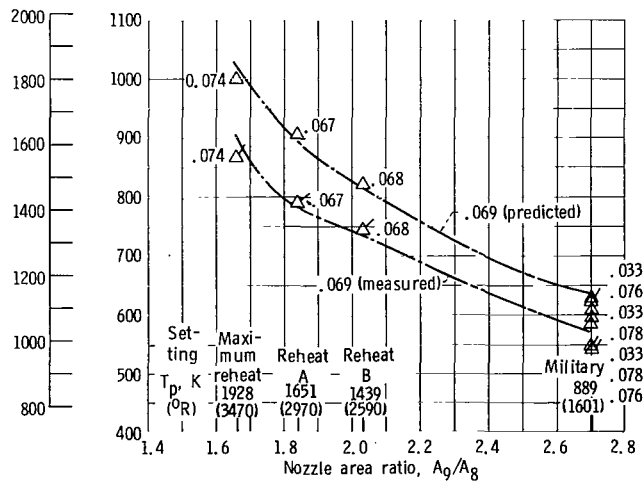
Figure 26. - Comparison of calculated and experimental data for impingement overexpanded flow. Reheat B; nozzle pressure ratio  $P_8/p_0$ , 2.9; corrected weight-flow ratio  $\omega\sqrt{T}$ , 0.029; secondary to primary total-pressure ratio  $P_5/P_8$ , 0.202; primary total temperature  $T_p$ , 1439 K (2590° R).



(a) Impingement flow.



(b) Nonimpingement flow.



(c) Unattached flow.

Figure 27. - Comparison of predicted wall temperature at point of maximum measured wall temperature and measured maximum wall temperature at different nozzle area ratios and primary total temperatures.

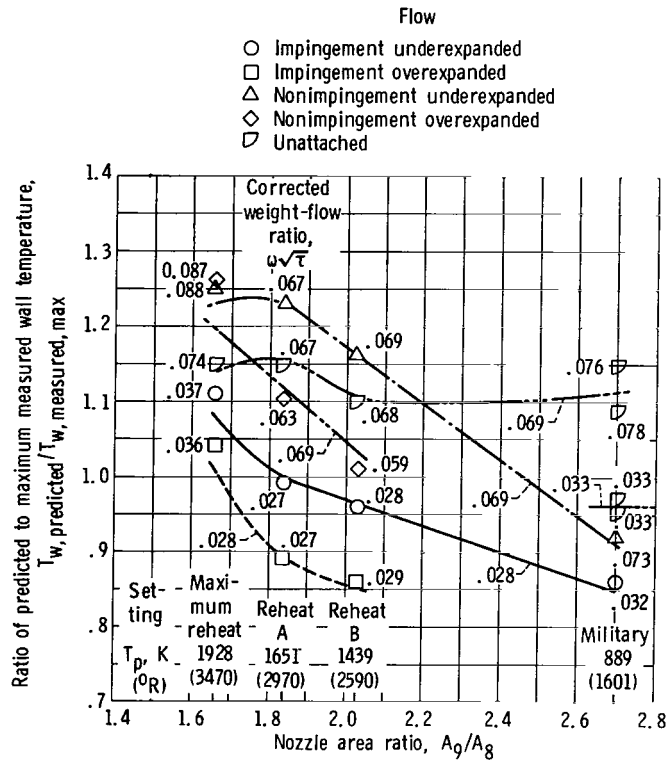


Figure 28. - Ratio of predicted wall temperature at point of maximum measured wall temperature to maximum measured wall temperature at different nozzle area ratios and primary total temperatures.

NATIONAL AERONAUTICS AND SPACE ADMINISTRATION  
WASHINGTON, D. C. 20546

OFFICIAL BUSINESS  
PENALTY FOR PRIVATE USE \$300

FIRST CLASS MAIL



POSTAGE AND FEES PAID  
NATIONAL AERONAUTICS AND  
SPACE ADMINISTRATION

005 001 C1 U 28 710806 S00903DS  
DEPT OF THE AIR FORCE  
AF SYSTEMS COMMAND  
AF WEAPONS LAB (WLOL)  
ATTN: E LOU BOWMAN, CHIEF TECH LIBRARY  
KIRTLAND AFB NM 87117

POSTMASTER: If Undeliverable (Section 158  
Postal Manual) Do Not Return

*"The aeronautical and space activities of the United States shall be conducted so as to contribute . . . to the expansion of human knowledge of phenomena in the atmosphere and space. The Administration shall provide for the widest practicable and appropriate dissemination of information concerning its activities and the results thereof."*

— NATIONAL AERONAUTICS AND SPACE ACT OF 1958

## NASA SCIENTIFIC AND TECHNICAL PUBLICATIONS

**TECHNICAL REPORTS:** Scientific and technical information considered important, complete, and a lasting contribution to existing knowledge.

**TECHNICAL NOTES:** Information less broad in scope but nevertheless of importance as a contribution to existing knowledge.

**TECHNICAL MEMORANDUMS:** Information receiving limited distribution because of preliminary data, security classification, or other reasons.

**CONTRACTOR REPORTS:** Scientific and technical information generated under a NASA contract or grant and considered an important contribution to existing knowledge.

**TECHNICAL TRANSLATIONS:** Information published in a foreign language considered to merit NASA distribution in English.

**SPECIAL PUBLICATIONS:** Information derived from or of value to NASA activities. Publications include conference proceedings, monographs, data compilations, handbooks, sourcebooks, and special bibliographies.

**TECHNOLOGY UTILIZATION PUBLICATIONS:** Information on technology used by NASA that may be of particular interest in commercial and other non-aerospace applications. Publications include Tech Briefs, Technology Utilization Reports and Technology Surveys.

*Details on the availability of these publications may be obtained from:*

**SCIENTIFIC AND TECHNICAL INFORMATION OFFICE**

**NATIONAL AERONAUTICS AND SPACE ADMINISTRATION**

**Washington, D.C. 20546**